

**TIRE MODEL IDENTIFICATION AND DEVELOPMENT OF A
TIRE-ROAD FRICTION OBSERVER**

A Thesis
Presented to
The Academic Faculty

By

Julius Kortenbruck

In Partial Fulfillment
Of the Requirements for the Degree
Mechanical Engineering in the
George W. Woodruff School of Mechanical Engineering

Georgia Institute of Technology
August 2019

COPYRIGHT © JULIUS KORTENBRUCK 2019

TIRE MODEL IDENTIFICATION AND DEVELOPMENT OF A TIRE-ROAD FRICTION OBSERVER

Approved by:

Dr. Panagiotis Tsiotras, Advisor
School of Aerospace Engineering
Georgia Institute of Technology

Prof. Dr.-Ing. Dr. h.c. Oliver Sawodny
Institute for System Dynamics
University of Stuttgart

Dr. Michael J. Leamy
School of Mechanical Engineering
Georgia Institute of Technology

Prof. Dr.-Ing. Cristina Tarín
Institute for System Dynamics
University of Stuttgart

Dr. Aldo A. Ferri
School of Mechanical Engineering
Georgia Institute of Technology

Date Approved: July 24, 2019

TABLE OF CONTENTS

List of Tables	III
List of Figures	IV
List of Symbols and Acronyms	VI
Summary	XI
1 Introduction	1
1.1 Motivation.....	1
1.2 Literature Review	2
2 Vehicle Models and Observer	5
2.1 Reference Vehicle Model.....	5
2.2 Simplified Vehicle Dynamic Models	8
2.2.1 Single Track Model.....	9
2.2.2 Tire Model.....	13
2.3 Extended Kalman Filter.....	18
2.3.1 Algorithm.....	19
2.3.2 Observer Design.....	24
2.3.3 Observability	27
3 Tire and EKF Parameter Identification	29
3.1 Gradient Based Optimization	29
3.2 Error Definition for Gradient Based Optimization	33
3.3 Maneuvers	34
3.3.1 Coast-Down Test.....	35
3.3.2 Dynamic Maneuvers	36
4 Results	43
4.1 Tire Identification.....	43
4.1.1 Inconsistency within the Reference Vehicle Model.....	50
4.2 EKF Parameter Identification	53

4.3	Verification.....	58
4.3.1	Justification for Maneuver Choice	62
5	Conclusions	65
	Appendix	67
A.1	All Results Tire Identification	67
A.2	All Results EKF Identification.....	71
	References	76

LIST OF TABLES

Table 1: Basic vehicle model properties	8
Table 2: Standard deviation of measurement noise	26
Table 3: Initial values and bounds for tire model identification	31
Table 4: Initial values and bounds of identification of Q	32
Table 5: Scaling for tire parameter optimization	34
Table 6: Resistance parameters.....	35
Table 7: Overview parameters lateral maneuver	39
Table 8: Maximal reached slip angle during dynamic maneuvers	39
Table 9: Max longitudinal slip values for emergency braking	40
Table 10: Resulting tire parameters front and rear	48

LIST OF FIGURES

Figure 1: Coordinate systems and most relevant dimensions of reference vehicle model	7
Figure 2: Single-track model	10
Figure 3: Force-slip relationship of the Pacejka tire model [10].....	14
Figure 4: Characteristics of Henning tire model [4]	17
Figure 5: General principle of an observer	19
Figure 6: Resulting observer design.....	27
Figure 7: Steering input profile dynamic maneuvers	38
Figure 8: Acceleration profile for emergency braking	40
Figure 9: Result of tire identification for semi-steady-state circle on $\mu = 1$	44
Figure 10: Result of tire identification for constant sine wave on $\mu = 1$	45
Figure 11: Result of tire identification for braking maneuver on $\mu = 1$	46
Figure 12: Influence of normal force on front axle behavior with $F_z = 8 \text{ kN}, 6 \text{ kN}, 4 \text{ kN}$ on $\mu = 1$	47
Figure 13: Influence of change in μ on front axle behavior on $\mu = 1, 0.7, 0.4$ with $F_z = 6 \text{ kN}$	47
Figure 14: Influence of normal force on rear axle behavior with $F_z = 8 \text{ kN}, 6 \text{ kN}, 4 \text{ kN}$ on $\mu = 1$	48
Figure 15: Influence of change in μ on rear axle behavior on $\mu = 1, 0.7, 0.4$ with $F_z = 6 \text{ kN}$	48
Figure 16: Lateral tire forces during sine wave maneuver between 8s-9s with a) front tire and b) rear tire.....	49
Figure 17: Normalized lateral tire forces during sine wave maneuver between 8s-9s with a) front tire and b) rear tire.....	50
Figure 18: Normal force on a) front axle and b) rear axle for real vehicle and single-track model during sine wave maneuver	52
Figure 19: Lateral forces on a) front and b) rear axle during constant sine wave maneuver.....	53
Figure 20: Result of μ estimation for steady-state-circle on $\mu = 1$	55
Figure 21: Result of μ estimation for constant sine wave maneuver on $\mu = 1$	56
Figure 22: Result of μ estimation for braking maneuver on $\mu = 1$	57

Figure 23: Steering angle first verification maneuver.....	58
Figure 24: Result estimation process first validation maneuver.....	59
Figure 25: Steering profile for second verification maneuver.....	60
Figure 26: Result estimation process second validation maneuver.....	61
Figure 27: Performance of μ estimation on $\mu = 0.4$ when identification is only done on high friction surface.....	63
Figure 28: Performance of estimating μ during original maneuver, when identification of tire and EKF is done with maneuvers with reduced speed.....	64
Figure 29: Results of identification for sine chirp maneuver on $\mu = 1$	67
Figure 30: Results of identification for Semi-Steady-State circle on $\mu = 0.4$	68
Figure 31: Results of identification for constant sine wave maneuver on $\mu = 0.4$	68
Figure 32: Results of identification for sine chirp maneuver on $\mu = 0.4$	69
Figure 33: Results of identification for emergency braking maneuver on $\mu = 0.4$	70
Figure 34: Results of μ estimation for sine chirp maneuver on $\mu = 1$	71
Figure 35: Results of μ estimation for semi-steady-state circle maneuver on $\mu = 0.4$	72
Figure 36: Results of μ estimation for constant sine wave maneuver on $\mu = 0.4$	73
Figure 37: Results of μ estimation for sine chirp maneuver on $\mu = 0.4$	74
Figure 38: Results of μ estimation for emergency braking maneuver $\mu = 0.4$	75

LIST OF SYMBOLS AND ACRONYMS

Acronym	Meaning
MF	Magic Formula
CoG	Center of Gravity
KF	Kalman Filter
EKF	Extended Kalman Filter

Variable	Unit	Description
μ	-	Coefficient of friction
μ_{\max}	-	Maximal potential of coefficient of friction
μ_{use}	-	Utilized coefficient of friction
X_E	-	X-axis of earth coordinate system
Y_E	-	Y-axis of earth coordinate system
Z_E	-	Z-axis of earth coordinate system
X_V	-	X-axis of vehicle coordinate system
Y_V	-	Y-axis of vehicle coordinate system
Z_V	-	Z-axis of vehicle coordinate system
X_W	-	X-axis of wheel coordinate system
Y_W	-	Y-axis of wheel coordinate system
Z_W	-	Z-axis of wheel coordinate system
X_T	-	X-axis of tire coordinate system
Y_T	-	Y-axis of tire coordinate system
Z_T	-	Z-axis of tire coordinate system
l_f	m	Distance from center of gravity to front axle
l_r	m	Distance from center of gravity to rear axle
h	m	Distance from center of gravity to ground
x	-	Vehicle state vector
u	-	Vehicle input vector
$\dot{\psi}$	$\frac{\text{rad}}{\text{s}}$	Vehicle yaw rate
v_x	$\frac{\text{m}}{\text{s}}$	Vehicle speed along x-axis of vehicle coordinate system

Variable	Unit	Description
v_y	$\frac{\text{m}}{\text{s}}$	Vehicle speed along y-axis of vehicle coordinate system
a_x	$\frac{\text{m}}{\text{s}^2}$	Vehicle acceleration along x-axis of vehicle coordinate system
δ	rad	Wheel steering angle
ω_F	$\frac{\text{rad}}{\text{s}}$	Wheel speed front
ω_R	$\frac{\text{rad}}{\text{s}}$	Wheel speed rear
I_z	kgm^2	Vehicle inertia about z-axis of vehicle coordinate system
m	kg	Total vehicle mass
F_{Fx}	N	Longitudinal tire force at front
F_{Fy}	N	Lateral tire force at front
F_{Rx}	N	Longitudinal tire force at rear
F_{Ry}	N	Lateral tire force at rear
F_{Res}	N	Driving resistance forces
T_a	-	Time constant longitudinal acceleration
d_1	N	Constant resistance parameter
d_2	$\frac{\text{N}}{\text{m/s}}$	Linear resistance parameter
d_3	$\frac{\text{N}}{\text{m/s}^2}$	Quadratic resistance parameter
\bar{B}	-	Stiffness factor
\bar{C}	-	Shape factor
\bar{D}	-	Peak factor

Variable	Unit	Description
\bar{E}	-	Factor of curvature
S_v	-	Vertical Shift
S_h	-	Horizontal Shift
α	rad	Slip angle
κ	-	Longitudinal slip
$v_{T,x}$	$\frac{m}{s}$	X-velocity in tire frame
$v_{T,y}$	$\frac{m}{s}$	Y-velocity in tire frame
r_W	m	Wheel radius
F_{max}	N	Maximum of tire force
F_z	N	Tire normal load
k_{F_z}	-	Load scaling factor
F_{z0}	N	Nominal normal force
k_κ	-	Longitudinal tire stiffness scaling factor
$k_{\mu x}$	-	Maximal longitudinal tire force scaling factor
λ	-	Combined slip
A	-	State space matrix
B	-	Control matrix
C	-	Measurement matrix
w	-	Process noise term
v	-	Measurement noise term
Q	-	Process noise covariance
R	-	Measurement noise covariance

Variable	Unit	Description
\hat{x}	-	State estimate
\hat{y}	-	Virtual measurement
K	-	Kalman gain
P	-	Error Covariance
Ob	-	Observability matrix
N_m	-	Number of maneuvers
N_x	-	Number of states
n	-	Number of timesteps

SUMMARY

In order to improve vehicle safety systems and autonomous control of vehicles, the real time knowledge of tire forces and friction coefficient is desirable. The tire interaction with the road through the tire contact patch is the only means to control the movement of the vehicle.

The goal of this thesis is to develop a nonlinear observer for estimation of the potential of the road friction coefficient during various driving maneuvers. Maneuvers will be performed by a nonlinear 14 degree of freedom vehicle model with independent suspension, which serves as a substitute for a physical vehicle. An Extended Kalman filter is chosen as the observer. Within the observer, the reference vehicle is represented by a nonlinear single-track model. The tire model used is a modified version of the widely known Pacejka Magic Formula tire model. To identify the parameters for the tire model, a gradient based minimization problem is solved to find the tire parameters such that the dynamic characteristics of the single-track model closely match those of the reference vehicle.

Once the tire parameters are determined, a similar minimization problem is set up and solved to obtain the parameters for the Extended Kalman Filter. Parameters of the EKF are chosen such that the state estimation closely matches a reference measurement from the complex vehicle simulation model.

The resulting observer shows good performance in estimating the friction coefficient during highly nonlinear maneuvers. Some maneuvers are performed that show the estimation of varying road conditions. The performance is governed by the quality of the

tire model. When the observer model shows poor performance in capturing the behavior of the reference vehicle, the estimation of the friction coefficient suffers. If the tire is operated in the linear region, the friction coefficient is harder to identify. Improvements in future work can be made by carefully selecting the maneuvers for identifying the tire model, such that a broader range of tire slip and normal load variations is reached.

1 INTRODUCTION

1.1 Motivation

All relevant forces to control a road vehicle are transmitted through the contact patch between the tires and the road. Systems that allow for control of the path of the vehicle such as steering or braking and active systems that contribute to vehicle safety such as anti-lock braking, anti-slip control, or an electronic stabilization system are trying to fully utilize the potential of the force between tire and road. Just as an experienced driver would change his driving based on whether he is driving on a surface such as dry tarmac or snow, the active safety systems can also apply the proper control strategy using knowledge about the road conditions. The potential for the force that can be transmitted is, amongst other things, governed by the tire-road friction coefficient μ . For every instance and operating condition there is a maximal potential friction coefficient μ_{\max} and an actually utilized μ_{use} . Under ideal conditions, the active systems could, with knowledge of μ_{\max} , control the vehicle such that $\mu_{\text{use}} = \mu_{\max}$. This would maximize the force that is transferred through the tire contact patch. Therefore, knowledge of μ_{\max} is desirable. Even though μ_{\max} depends on a plethora of outside factors, such as normal load, tire temperature, road surface, relative tire velocity, tire position relative to road, or rubber compound to just name a few, it can be identified using a suitable tire model and knowledge of the operating conditions of the tire. In order to develop a system that is able to identify the friction potential under the current driving situation, a vehicle and tire model is needed. While a simple vehicle model is easily obtained with knowledge of basic geometrical data and mass properties of the vehicle, parameters for a tire model are not as easily available. This can be a limiting factor when

it comes to small research and development groups that do not have the necessary resources for tire testing. Furthermore, research on advanced driver assistance systems is sometimes conducted using small scale vehicle models. It is therefore desirable to find a method that allows for development of algorithms to estimate the friction potential with limited knowledge of the vehicle and tire.

1.2 Literature Review

Designing a tire-road friction estimator is something that has been of interested to the academic world and the vehicle industry for a considerable amount of time. A comprehensive study about different methods and a comparison of recent works on the subject has been done by [1]. Here, and in many other works on the topic, the ways of determining the friction coefficient are split up in caused-based methods and effect-based methods, where caused-based methods denote those methods that identify the friction coefficient through analyzation of the environment. This includes road surface roughness, level of lubrication (rain, snow), ambient temperature, and so on. Effect-based methods identify the friction potential through the effect that a change in tire-road friction has on the vehicle behavior. The general benefit of the latter method is that it can usually be done without expensive measurement equipment that is necessary to analyze environmental factors on the coefficient of friction. For this reason, effect-based methods are the preferred options. Numerous people have worked on such methods and an overview of some of them will be conducted to establish what sets this work apart from what has been done before.

A powerful joint observer for the parameters of a Pacejka tire model and vehicle states has been designed by [2]. While the car drives on an oval track with a loose surface, tire

parameters and vehicle states are estimated online in conjunction with each other. While it proves to be a very powerful observer for vehicle state estimation, the resulting tire model has limited validity, as it is only valid within the slip region that is reached during the initial phase of maneuver performance where the tire parameters are estimated. It remains unknown whether or not the resulting tire model would be valid under different driving conditions. While [3] designs an observer to estimate friction during longitudinal and lateral maneuvers, the tire model is already assumed to be known from the simulation environment that the work is conducted with. A tire-road friction observer is designed by [4] and a tire model based on the Pacejka tire model is derived for this task. While ultimately the same tire model is used within this work, the parameters for the model used in [4] are taken from a database provided by tire manufacturer. While [5] and [6] demonstrated methods to estimate parameters for a Pacejka tire model without extensive measurement equipment, there are some practical limitations to these identification processes. They are done online and during regular driving operations, intended such that the driver does not notice it. This results in the validity of the resulting models not reaching far into the nonlinear region of the tire. This would not allow for usage of the resulting tire model as a base for a tire-road friction observer for highly dynamic driving operations. A publication most similar to what is intended for this work comes from [7]. Here, selected maneuvers are performed to identify the tire parameters. Parameters are identified online and offline and it is concluded that the offline identification yields better results. The resulting model is used to successfully design a tire-road friction observer. However, the tire model is a linear model, which limits the tire road friction estimation to maneuvers in the linear region of tire behavior. To the author's knowledge, no work has been conducted

to identify nonlinear tire parameters with carefully selected maneuvers that ensures validity into high slip regions without external measurement equipment and then using the model to build a tire-road friction estimator. Successful completion of this work would allow small research teams to work on friction observers, without having access to tire data or measurement equipment to derive such data (e.g. force measuring wheels).

2 VEHICLE MODELS AND OBSERVER

In this chapter, all necessary vehicle models are introduced. Furthermore, the observer that is used to solve the estimation problem is designed.

2.1 Reference Vehicle Model

A simulated vehicle with 14 degrees of freedom serves as a reference and as a stand-in for a physical vehicle. For the rest of this work this vehicle is referred to as “real vehicle.” The model is part of the simulation environment of the MATLAB/SIMULINK[®] software package (Release 2018a). All information about the vehicle, the tire model used, and configuration are taken from the software documentation [8]. The model consists of a rigid body with six degrees of freedom, which are longitudinal, lateral, and vertical displacement and roll, pitch, and yaw. Roll, pitch, and yaw describe the rotation of the vehicle body about the X_V , Y_V , and Z_V axis of the vehicle body coordinate system. Each wheel has one rotational degree of freedom and can translate vertically. The movement of the vehicle and wheels are described with four different coordinate systems as defined in ISO8855. All coordinate systems are Cartesian coordinate systems and listed below.

- Earth fixed (inertial) coordinate system (X_E, Y_E, Z_E): Gravity is acting in the direction of negative Z_E . The plane spanned by X_E, Y_E is parallel to the ground plane.
- Vehicle fixed coordinate system (X_V, Y_V, Z_V): Placed at the center of gravity of the vehicle body with X_V pointing towards the front of the vehicle parallel to the vehicle

plane of symmetry and Z_V is pointing upwards. Movement of the vehicle is described as the movement of the vehicle fixed coordinate system about the earth fixed coordinate system.

- Wheel fixed coordinate system (X_W, Y_W, Z_W): Fixed to the wheel with the origin placed at the wheel center where X_W is parallel to the wheel plane of symmetry and Y_W is parallel to the wheel spin axis. Z_W is pointing upwards.
- Tire fixed coordinate system (X_T, Y_T, Z_T): Each tire has a coordinate system with the origin placed at the contact point of the tire with the ground. The plane spanned by X_T, Y_T is parallel to the ground plane, orientation of X_T is defined by the intersection of the wheel plane and the road plane, and Z_T is pointing upwards.

The position of the coordinate systems and the basic dimensions of the vehicle are shown in Figure 1. For easier readability, only the wheel and tire coordinate system of the rear right are shown. By standard configuration, the vehicle is equipped with a solid axle suspension at the rear and independent suspension at the front.

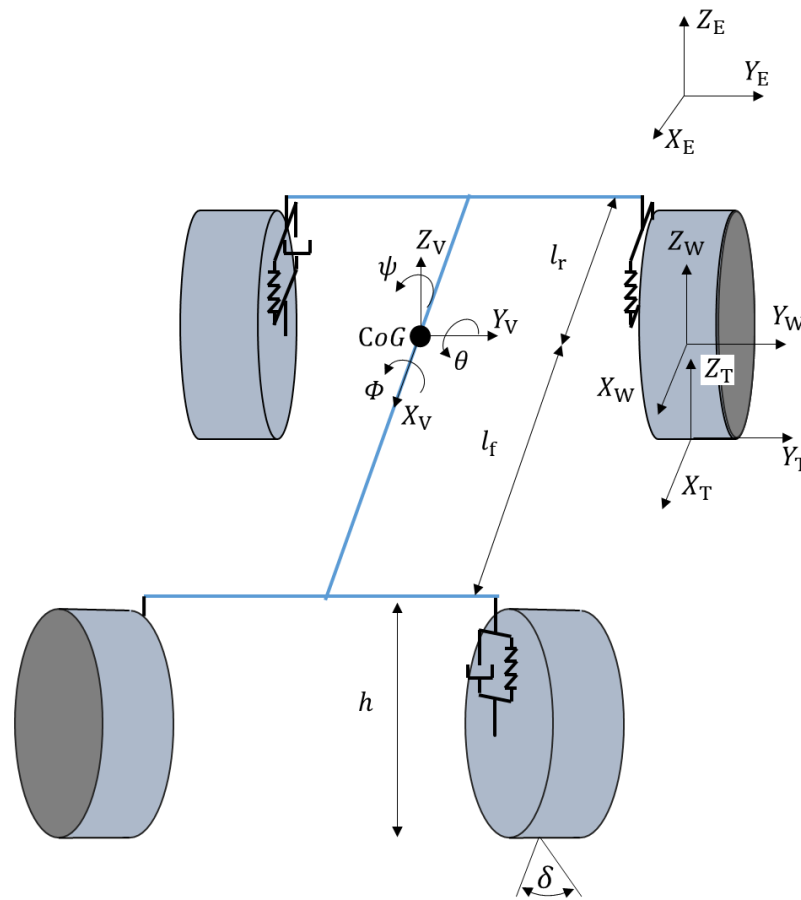


Figure 1: Coordinate systems and most relevant dimensions of reference vehicle model

The most relevant vehicle parameters are listed in Table 1. These are also used to set up the observer model, which is described in the following chapter.

Table 1: Basic vehicle model properties

Property	Value	Unit
Sprung Vehicle Body Mass	1096.7	<i>kg</i>
Unsprung Mass per Wheel	22.0693	<i>kg</i>
Inertia about Z_V	2066	<i>kg m²</i>
Distance CoG to Front Axle (l_f)	1.7258	<i>m</i>
Distance CoG to Rear Axle (l_r)	1.3492	<i>m</i>
Height CoG (h)	0.437	<i>m</i>
Unloaded Wheel Radius	0.309	<i>m</i>

The tire model used is a MF-Tyre 6.2 tire model. Based on the inputs, the model returns the tire deflection and forces and moments for all six degrees of freedom. This model can capture the effects of camber angle, relative velocity in the contact patch, inflation pressure, normal load, relaxation length, combined slip, changing effective rolling radius, and tire damping and stiffness.

2.2 Simplified Vehicle Dynamic Models

The model used in the observer to represent the real vehicle consists of a nonlinear single-track model with a modified Magic Formula (MF) tire model on each axle. The single-track model has been chosen for simplicity and it has been shown to produce good results for vehicle state and tire force estimation in [9] and [2]. The tire model is a relatively new

variation of the MF model and has been shown to be suitable for the tire force and friction coefficient estimation in [4].

2.2.1 *Single Track Model*

The information about the principles of the single-track model are taken from [10]. A nonlinear single-track model, or “bicycle model,” allows for representation of the longitudinal and lateral behavior of a car with reduced computational effort compared to a full vehicle model. The main characteristic of a single-track model is that the tires on each axle are merged into one representative tire in the center. Several other simplifications are also applied:

- Neglecting of roll and pitch dynamics
- No suspension dynamics
- No inertia about longitudinal or lateral axis of the vehicle.
- Rigid steering
- Wheels without inertia
- Zero road bank angle

These reduce the dynamic states of the vehicle model and allow for reduced computational effort.

The movement of the single-track model is described with three different coordinate systems. They are an earth fixed, a vehicle fixed, and a tire fixed coordinate system. They follow the same definitions as the coordinate systems introduced in Chapter 2.1. The properties and dynamic states of the single-track model are displayed in Figure 2.

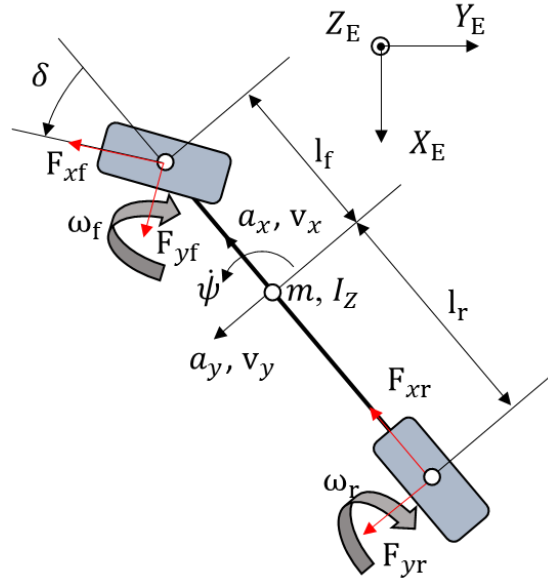


Figure 2: Single-track model

The simplifications of the single-track model such as rigid steering or the absence of load transfer in the lateral direction mean that the tire model of the single track model does not only represent the tire of the real vehicle but also underlying effects of compliance in the steering and the nonlinear effect of load transfer within one axle. Hence, the tire model of the single-track model does not represent the characteristics of each tire but rather each axle of the real vehicle.

To be used in the observer model, the vehicle is described with a set of nonlinear equations of the following form:

$$\dot{x} = f(x, u) \tag{2.1}$$

with the state variable vector

$$x = \begin{bmatrix} \psi \\ v_x \\ v_y \\ a_x \end{bmatrix} \quad (2.2)$$

and the differential equations

$$\ddot{\psi} = \frac{(F_{Fx} \cdot \sin \delta + F_{Fy} \cdot \cos \delta) l_F + F_{Ry} \cdot l_R}{I_z} \quad (2.3)$$

$$\dot{v}_x = \frac{(F_{Fx} \cos \delta - F_{Fy} \sin \delta + F_{Rx} - F_{Res})}{m} + v_y \dot{\psi} \quad (2.4)$$

$$\dot{v}_y = \frac{(F_{Fx} \sin \delta + F_{Fy} \cos \delta - F_{Ry})}{m} - v_x \dot{\psi} \quad (2.5)$$

$$\dot{a}_x = \frac{1}{T_a} \left(\frac{(F_{Fx} \cos \delta - F_{Fy} \sin \delta + F_{Rx} - F_{Res})}{m} - a_x \right) \quad (2.6)$$

In the above equations, m denotes the vehicle mass, I_z is the moment of inertia about the vertical axis at the center of gravity, δ is the steering angle of the front wheel, and v_x and v_y are the vehicle velocities in the body frame. The tire friction forces are described by $F_{i,j}$ with $i = F, R$ denoting the position at front or rear and $j = x, y$ the direction within the wheel coordinate system. F_{Res} is a force that captures driving resistance through effects like rolling resistance of the tire and aerodynamic drag. It is calculated according to

$$F_{\text{Res}} = d_1 + d_2 \cdot v_x + d_3 \cdot v_x^2 \quad (2.7)$$

where d_1 is a constant resisting force, d_2 allows for a resistance that is linearly dependent on the vehicle velocity (i.e. tire rolling resistance), and d_3 captures effects such as aerodynamic drag. The parameters d_1 , d_2 , and d_3 are identified with a free-rolling coast down maneuver from high speeds as explained in Chapter 3.3.1.

The longitudinal acceleration a_x is included in the state space to be able to capture the effects of longitudinal acceleration on the load transfer. T_a is a small constant, chosen according to [4], in order to give the rate of change of acceleration the dynamics of a first order system.

The control variables are given as

$$u = \begin{bmatrix} \delta \\ \omega_F \\ \omega_R \end{bmatrix} \quad (2.8)$$

where δ is the wheel steering angle and ω_F and ω_R are the wheel speeds of the front and rear axle respectively. Despite the real vehicle being controlled using a torque input or, for that matter, a typical physical car being controlled using a throttle input from the driver, the wheel speed is chosen as the control input for the observer model. This allows for reduced complexity of the model, as there is no need to model a powertrain or braking system to translate a throttle/brake input into a torque applied at the wheel.

2.2.2 *Tire Model*

In the following subchapter, the tire model used is introduced. It is a modification of the Magic Formula (MF) tire model. The Magic Formula tire model stems from the work of Hans. B. Pacejka and the equations and explanations are according to [10], while the modified model used here comes from the doctoral thesis of Kay-Uwe Henning [4].

The MF tire model is a widely used way to model tire behavior and it is not based on an underlying physical model but rather a mathematical description to fit experimental tire data of a slip-force relationship for quasi-static operating conditions. It was first introduced by Pacejka in 1992 and has since seen several revisions to allow for a broader representation of tire behavior. The model which was first introduced is

$$y = \bar{D} \cdot \sin[\bar{C} \cdot \arctan(\bar{B} \cdot x - \bar{E} \cdot [\bar{B} \cdot x - \tan^{-1}(\bar{B} \cdot x)])] \quad (2.9)$$

It allows for modeling of lateral and longitudinal tire forces as well as the self-aligning torque of the tire.

This leads to the following slip-force relationship.

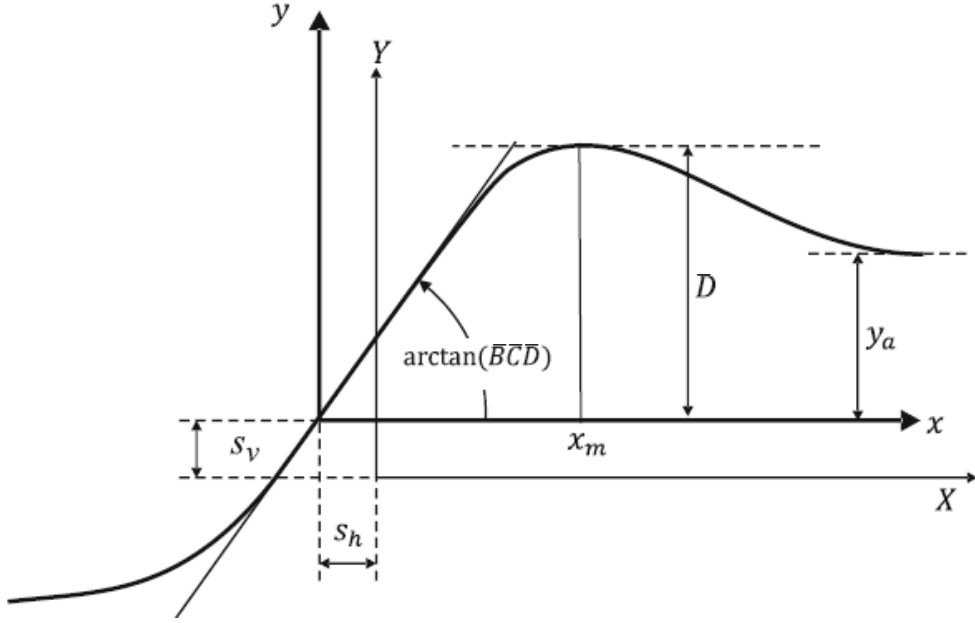


Figure 3: Force-slip relationship of the Pacejka tire model [10]

Here, y denotes the resulting tire force or tire self-aligning moment under the normal load F_z with x as the input parameter either being the longitudinal slip κ or sideslip angle α of the tire. The factor D represents the achievable maximum. The initial slope of the linear region of tire behavior is governed by $\tan^{-1}(\overline{BCD})$. \overline{B} is known as a stiffness factor, \overline{C} as a shape factor, and \overline{E} as the factor of curvature. The slip angle α and slip ratio κ are given by

$$\alpha = \tan^{-1} \left(\frac{v_{T,y}}{v_{T,x}} \right) \quad (2.10)$$

$$\kappa = \frac{r_W \cdot \omega_W - v_{T,x}}{|v_{T,x}|} \quad (2.11)$$

where $v_{T,j}$ with $j = x, y$ is the velocity in the tire coordinate system, r_W is the radius of the wheel, and ω_W is the rotational speed of the wheel. The tire model allows for a computationally efficient representation of a wide array of tire operating points.

A horizontal or vertical shift of the resulting force output allows for representation of rolling resistance or the influence of tire camber [10]. This leads to the following form:

$$Y = y + S_v \quad (2.12)$$

$$x = X + S_h \quad (2.13)$$

$$y = S_v + \bar{D} \cdot \sin[\bar{C} \tan^{-1}(\bar{B} \cdot (x + S_h) - \bar{E} \dots \cdot [\bar{B} \cdot (x + S_h) - \tan^{-1}(\bar{B} \cdot (x + S_h))])]] \quad (2.14)$$

However, this model does neglect many aspects of tire behavior such as dependency on tire pressure, relative velocity between tire and road, effective rolling radius, camber angle of the tire, and nonlinear dependency of the normal load. Furthermore, a scaling of the transmittable tire forces, based on the friction coefficient of the surface, is needed to be able to identify the friction coefficient with an estimation process. In the doctoral thesis of Henning ([4]), a modified Pacejka tire model is introduced. It captures the effects that [4] claims to be the most relevant, but still is a simpler description of the tire behavior than other significantly more complex and computationally intensive tire models.

The model from [4] includes

- Nonlinear dependency of normal load
- Cross-correlation between longitudinal and lateral slip
- Dependency on road friction coefficient
- Difference in longitudinal and lateral tire stiffness
- Difference in maximal transferable load in longitudinal and lateral direction

The maximal transferrable lateral tire force is calculated with the parameters peak factor \bar{D} , the maximal longitudinal load scaling factor k_{F_z} and the normalized normal force F_{z0} and is linearly dependent on the friction coefficient μ and nonlinearly dependent on the acting normal force F_z .

$$F_{\max} = \bar{D}\mu F_z \left(1 + k_{F_z} \left(1 - \frac{F_z}{F_{z0}} \right) \right) \quad (2.15)$$

With knowledge of the longitudinal slip and the slip angle, the combined total slip can be calculated.

$$\lambda_x = k_\kappa \kappa \quad (2.16)$$

$$\lambda_y = \alpha \quad (2.17)$$

$$\lambda = \sqrt{\lambda_x^2 + \lambda_y^2} \quad (2.18)$$

where k_κ is a scaling factor for the longitudinal tire stiffness and α and κ are slip properties as introduced in (2.10) and (2.11).

With scaling for the maximal longitudinal tire force $k_{\mu x}$ and the factors \bar{B} and \bar{C} that were introduced with the Pacejka MF, the longitudinal and lateral tire force are calculated.

$$F_x = k_{\mu x} F_{\max} \sin \left(\bar{C} \tan^{-1} \left(\frac{\bar{B}}{\mu} \lambda \right) \right) \frac{\lambda_x}{\lambda} \quad (2.19)$$

$$F_y = -F_{\max} \sin \left(\bar{C} \tan^{-1} \left(\frac{\bar{B}}{\mu} \lambda \right) \right) \frac{\lambda_y}{\lambda} \quad (2.20)$$

The characteristics of the Henning model are shown in Figure 4. Here it is fitted to a Magic Formula Tire Model 5.2, which is comparable to the model used for the real vehicle. The difference in tire behavior due to changing μ is ultimately what allows for estimation of μ . The model by Henning shows a very good fit in the lateral behavior. The longitudinal behavior shows a discrepancy beyond the linear region of tire.

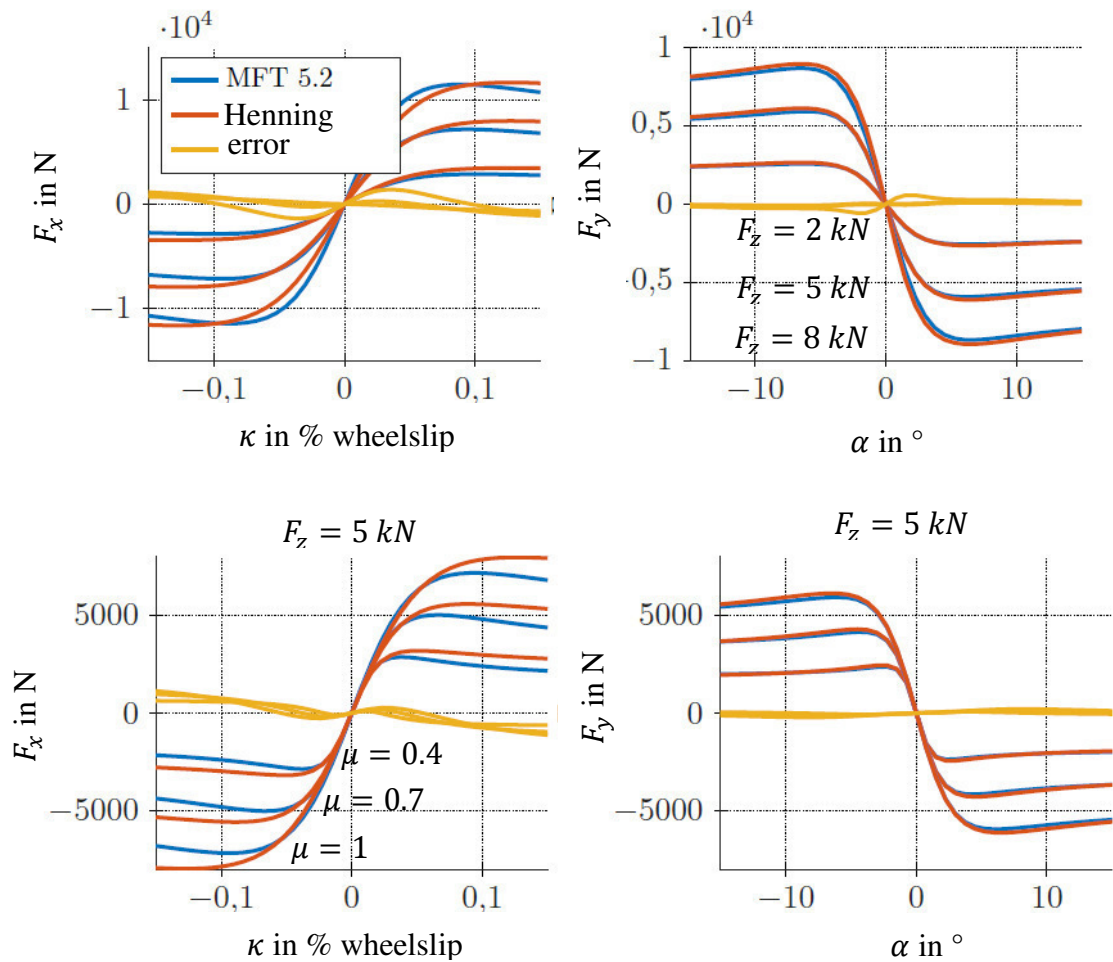


Figure 4: Characteristics of Henning tire model [4]

This discrepancy could potentially lead to issues when identifying the parameters for the longitudinal vehicle behavior. Nonetheless, the model has proven to be suitable for tire-road friction estimation in [4].

Each axle of the single-track model is parameterized with an individual set of tire parameters. This is necessary since the tire model of the single-track model represents the merged behavior of each axle. So even though the real vehicle is equipped with the same tires all around, the combined behavior of each axle is influenced by effects such as the load transfer in the lateral direction on each axle, effects of the suspension geometry, and the influence of the steering on the front axle. Namely, the simulation model, which serves as a real vehicle, is equipped with an independent front suspension with an anti-sway bar and a solid rear axle without an anti-sway bar. This leads to differences between the front and rear axle in lateral load transfer and to different rates of change of the tire camber angle under vehicle roll between the front and rear axle, just to name two examples. The camber angle denotes the angle between the wheel plane that is spanned by X_W and Z_W and the ground.

2.3 Extended Kalman Filter

In the following subchapter the observer used is introduced. First, the Extended Kalman Filter, the observer of choice, is derived. After that, an observer is designed and subsequently checked for observability. The equations and explanations of the subchapter 2.3.1 are based on [11].

2.3.1 Algorithm

The Kalman Filter (KF) is widely used in engineering applications for state estimation of dynamical systems. It allows for the estimation of internal states or parameters of a dynamical system based on external measurements. The system and the measurements can be disturbed by noise. In order to estimate states of a dynamical system, an observer model is needed that represents the dynamical system. The general flow of information for a state observer is depicted in Figure 5.

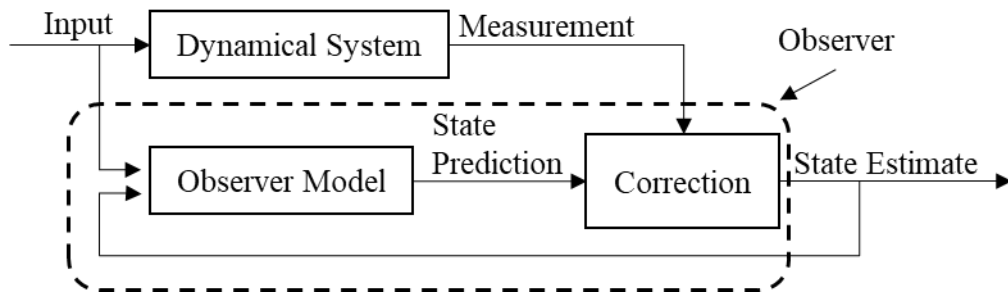


Figure 5: General principle of an observer

The observer model is a mathematical representation of the dynamical system and is driven with the same input as the dynamical system. This generates a prediction of the states of the system. The resulting states are transformed into a virtual measurement and the error between the virtual measurement and the measurements coming from the dynamical system are used to correct the state prediction resulting in the state estimate. The equations of the Kalman Filter are introduced with the example of a discrete linear time invariant observer model of the following form:

$$x_k = A \cdot x_{k-1} + B \cdot u_{k-1} + w_{k-1} \quad (2.21)$$

$$y_k = C \cdot x_k + v_k \quad (2.22)$$

Here, A is the state space matrix which transforms x_{k-1} to x_k and B is the control input matrix which relates the control input u_{k-1} to x_k . The matrix C relates the state vector x_k to the measurement vector y_k . The subscript k donates the current timestep. The noise, which is assumed to be random, white, and uncorrelated with zero mean is represented by w_k and v_k .

The covariance matrices of the noise terms are

$$E \cdot [w_k w_k^T] = Q_k \quad (2.23)$$

$$E \cdot [v_k v_k^T] = R_k \quad (2.24)$$

In practice, the process covariance matrix Q and measurement covariance matrix R are diagonal matrices because the states are assumed to be uncorrelated. The entries of Q and R are often chosen to be constant. If the noise behavior of the sensors is known, the matrix R is a matrix with the covariance of each sensor along its main diagonal. The process covariance matrix is more difficult to define as the covariance of process noise is generally unknown and is therefore subject to tuning. The larger the value in Q for a specific state, the lower the “trust” in the estimation of that state. A method for identifying the parameters for said matrix Q is presented in Chapter 3.

Each iteration of the Kalman Filter is split into a prediction and a correction step. In the prediction step the *a priori* estimate \hat{x}_k^- , the *a priori* error covariance P_k^- , and the virtual measurement \hat{y}_k are calculated by

$$\hat{x}_k^- = A \cdot \hat{x}_{k-1} + B \cdot u_{k-1}, \quad (2.25)$$

$$P_k^- = A P_{k-1} A + Q, \quad (2.26)$$

$$\hat{y}_k = C \cdot \hat{x}_k^- . \quad (2.27)$$

In the correction step, the Kalman gain and the *a posteriori* state estimate \hat{x}_k are calculated. The Kalman gain is applied to the difference of the virtual \hat{y}_k^- and real y_k measurements to “correct” the *a priori* state estimate \hat{x}_k^- .

$$K_k = P_k^- C^T (C P_k^- C^T + R)^{-1} \quad (2.28)$$

$$\hat{x}_k = \hat{x}_k^- + K_k (y_k - \hat{y}_k^-) \quad (2.29)$$

Lastly, the *a posteriori* error covariance P_k is obtained with

$$P_k = (I - K_k C) P_k^- \quad (2.30)$$

The filter has to be initialized with an initial error covariance $P_{k=0} = P_0$ and initial state estimate $\hat{x}_{k=0} = \hat{x}_0$. Here, the initial error covariance P_0 represents the user’s trust in the correctness of the initial state estimate \hat{x}_0 .

The Extended Kalman Filter

The use of the Kalman Filter is limited to linear models of dynamical systems. To use the principles and equations of the aforementioned Kalman Filter for nonlinear models, such as vehicle dynamic models, a linearization procedure must be included. The newfound filter is called the Extended Kalman Filter (EKF). A nonlinear system can be represented with

$$x_k = f(x_{k-1}, u_{k-1}) + w_{k-1} \quad (2.31)$$

$$y_k = h(x_k, u_k) + v_k \quad (2.32)$$

where $f(x_{k-1}, u_{k-1})$ and $h(x_k, u_k)$ are a set of nonlinear equations representing the system and the measurement model and w_k and v_k are independent, zero-mean, white Gaussian noise.

In order to use the equations (2.23) - (2.30), the nonlinear system is linearized by calculating the Jacobian at the current timestep with

$$F_k = \left. \frac{\partial f(x, u)}{\partial x} \right|_{x=\hat{x}_{k-1}, u=u_k} \quad (2.33)$$

$$H_k = \left. \frac{\partial h(x, u)}{\partial x} \right|_{x=\hat{x}_k^-, u=u_k} \quad (2.34)$$

which gives a matrix where the ij -th entry of F_k is the partial derivative of the i -th component of $f(x_k, u_k)$ with respect to the j -th component of the state vector x . The same principle applies for finding the linearization of the measurement model. The linearization is done around the most recent state estimate, which is \hat{x}_{k-1} for the linearization of the dynamical model and \hat{x}_k^- , so the *a priori* estimate, for the measurement model. Once the linearization is obtained, the prediction and correction step of the Kalman Filter are applied. For completeness and to avoid confusion with the linear Kalman Filter, the equations are repeated:

$$\hat{x}_k^- = f(\hat{x}_{k-1}, u_{k-1}) \quad (2.35)$$

$$P_k^- = F_k P_{k-1} F_k + Q \quad (2.36)$$

$$\hat{y}_k = h(\hat{x}_k^-, u_k) \quad (2.37)$$

$$K_k = P_k^- H_k^T (H_k P_k^- H_k^T + R)^{-1} \quad (2.38)$$

$$\hat{x}_k = \hat{x}_k^- + K_k (y_k - \hat{y}_k) \quad (2.39)$$

$$P_k = (I - K_k H_k) P_k^- \quad (2.40)$$

2.3.2 Observer Design

The Extended Kalman Filter uses the nonlinear single-track model and the state space description introduced in Chapter 2.2.1 for the observer model. The coefficient of friction μ is added as a state, so that it is part of the state space description to be estimated. Naturally, the change of μ does not follow any time dependent dynamic, so it follows that

$$\dot{\mu} = 0. \quad (2.41)$$

This leads to the state vector for the single-track model of

$$x = \begin{bmatrix} \psi \\ v_x \\ v_y \\ a_x \\ \mu \end{bmatrix}. \quad (2.42)$$

Since the differential equations of the single-track model are continuous, but the EKF is discrete, the model is discretized and integrated over every timestep. For this, the Euler-Forward scheme is chosen. This leads to:

$$x_k = f(x_{k-1}, u_{k-1}) = x_{k-1} + \dot{x}_{k-1} \cdot \Delta t \quad (2.43)$$

The differential equations for every state are listed in (2.3) - (2.6). The timestep Δt is chosen to be 0.01s, as 100 Hz is assumed to be a plausible sampling rate for commercially used sensors, based on [9].

The filter takes the averaged wheel steering angle δ and the averaged wheel speed of each axle ω_F and ω_R as an input as introduced in (2.8). Usually, an observer model takes the same control input as the plant that it is representing, but, to greatly simplify modelling of the nonlinear single-track model, the wheel speeds of the real vehicle are measured and used as the input to the single-track model.

The measurements taken from the real vehicle that are fed into the EKF are

$$y = \begin{bmatrix} \dot{\psi} \\ v_x \\ a_x \\ a_y \end{bmatrix}. \quad (2.44)$$

These are measurements that can be taken with onboard sensors that are available in modern cars. As the measurements taken from the simulation environment are ideal and noise free, a random white noise with Gaussian distribution is applied. The standard deviation of the noise is taken from [9] and is supposed to closely replicate the noise

characteristics of commercially available sensors in modern vehicles. The values are listed in Table 2.

Table 2: Standard deviation of measurement noise

Sensor variable	Standard deviation of noise
$\dot{\psi}$	$0.0035 \frac{1}{s}$
v_x	$0.2528 \frac{m}{s}$
a_x	$0.2266 \frac{m}{s^2}$
a_y	$0.2266 \frac{m}{s^2}$

The entries on the main diagonal of the measurement noise covariance matrix R are chosen based on the variance of the corresponding sensor signal, this is the squared standard deviation taken from Table 2. This leads to a diagonal 4 by 4 matrix with:

$$\text{diag}(R) = [0.0035^2 \quad 0.2528^2 \quad 0.2266^2 \quad 0.2266^2] \quad (2.45)$$

where $\text{diag}(R)$ are the entries on the main diagonal of R .

A measurement model $h(x_k, u_k)$ is needed to correlate the states of the single-track model to the measurements of the real vehicle. The measurement model is

$$\hat{y} = \begin{bmatrix} \hat{x}_1^- \\ \hat{x}_2^- \\ \hat{x}_4^- \\ \hat{x}_3^- + \hat{x}_1^- \cdot \hat{x}_2^- \end{bmatrix}. \quad (2.46)$$

which calculates the lateral acceleration of the single-track model through the relationship

$$a_y = \dot{v}_y + \psi \cdot v_x \quad (2.47)$$

The superscript $-$ denotes that the measurement model is based on the *a priori* estimate \hat{x}_k^- .

Note, that this requires another iteration of the observer model to calculate \dot{v}_y based on \hat{x}_k^- .

The final observer design is shown in Figure 6.

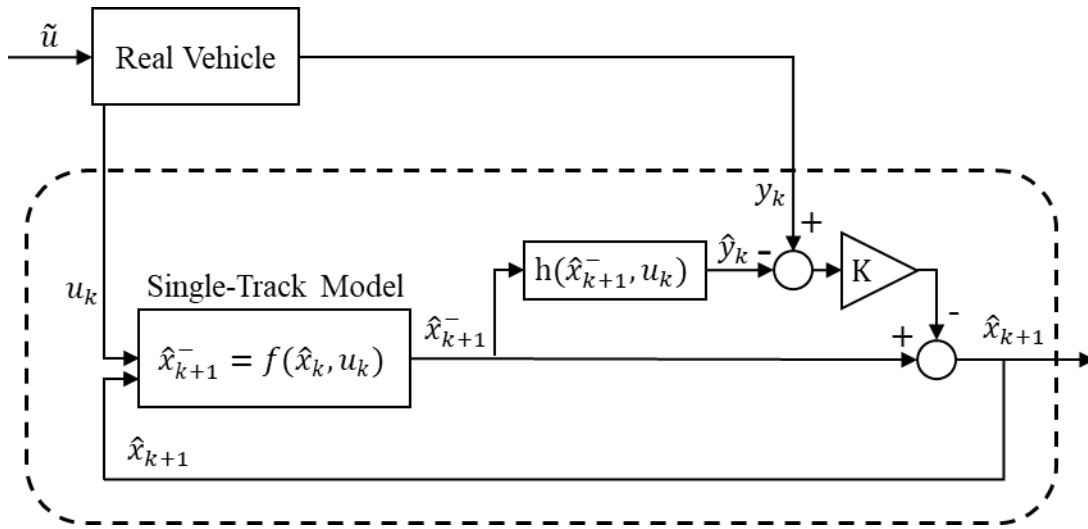


Figure 6: Resulting observer design

2.3.3 Observability

To be able to estimate the friction coefficient μ with the designed observer, the system needs to be observable.

According to [12], a linear time invariant system

$$\dot{x}_k = A \cdot x_k + B \cdot u_k, \quad (2.48)$$

$$y_k = C \cdot x_k, \quad (2.49)$$

is observable when within a finite interval $[t_0, t_1]$ the origin of the state vector $x(t_0)$ can be reconstructed from knowledge of the input $u(t)$ and output $y(t)$. In order to prove whether a linear system is observable, the Kalman rank criterion for observability is checked. It says that a system of dimension n is observable if, and only if, $rank(O_b) = n$, where

$$O_b = \begin{bmatrix} C \\ CA \\ CA^2 \\ \vdots \\ CA^{n-1} \end{bmatrix} \quad (2.50)$$

is the observability matrix.

Now, this criterion only proves observability for linear systems. Proving observability for nonlinear systems is a much more complicated task. How this can be done, using the concept of Lie derivatives, is described in [13].

For practical applications it is often enough to check for observability with the Kalman rank criterion by linearizing the system around certain points. To linearize the system the Jacobians are calculated as done in equations (2.33) - (2.34). While this is not a definite proof, it is often enough to check for observability at critical points with this method. In this case, such points could be the vehicle standing or driving in a straight line without a steering input. If the linearized system is observable, observability is assumed as long as there is no reason not to make this assumption. So as long as the designed observer shows the expected behavior, the system can be assumed observable, at least for the tested cases. For this reason, no further proof of observability is conducted for the system designed in Chapter 2.3.2.

3 TIRE AND EKF PARAMETER IDENTIFICATION

As the goal of this work is to design an observer for tire-road friction estimation without prior knowledge of a tire model, the parameters for the tire model of the observer model need to be identified. Furthermore, the process noise covariance matrix Q of the Extended Kalman Filter needs to be identified. The general principle for handling both of these tasks are the same. The parameters are identified by setting up a minimization problem where the parameters are chosen such that the error between the model behavior and a reference is minimized. The reference is noise free measurements taken from the real vehicle during the performance of dynamic driving maneuvers. First, the tire parameters are identified such that the dynamic behavior of the single-track model matches the behavior of the real vehicle as closely as possible. Secondly, the process noise covariance matrix Q is identified such that the result of the state estimation matches the measurements taken from the real vehicle as closely as possible. This includes the estimation of the friction coefficient μ . In the following subchapters the necessary tools for identifying the tire parameters and the process noise covariance matrix are introduced, which are the setup of the minimization problem, the error definition, and the dynamic maneuvers.

3.1 Gradient Based Optimization

To identify the parameters for the tire model and the Extended Kalman filter, the built in MATLAB[®] function *fmincon* is used. This function finds the minimum in a constrained nonlinear multivariable problem. The following subchapter is based on the software documentation [14]. The function *fmincon* finds a minimum of a problem formulated as

$$\min_s f(s) \text{ such that } \begin{cases} c(s) \leq 0 \\ ceq(s) = 0 \\ A \cdot s \leq b \\ Aeq \cdot s = beq \\ lb \leq s \leq ub \end{cases} \quad (3.1)$$

where $c(s) \leq 0$ and $ceq(s) = 0$ are a set nonlinear inequalities and equalities respectively and $A \cdot s \leq b$ and $Aeq \cdot s = beq$ are a set of linear inequality and equality conditions. The bounds lb and ub limit the design variable s . The variable s can be a scalar, vector, or matrix. The boundary conditions are used to limit the choice of s to plausible values chosen by the user (e.g. no values < 0). For identifying the tire parameters, the vector s consists of the set of tire parameters and for identifying the parameters of the Extended Kalman Filter s consists of the entries on the main diagonal of the matrix Q . The optimization function calls the model that is to be optimized and simulates it with the current set of parameters and returns a scalar value that represents the error between a reference model and the model that is to be tuned. The error is to be minimized. Different algorithms can be chosen for the *fmincon* function for the minimization. The default choice by MATLAB® is the ‘interior-point’ algorithm. Further information about this algorithm can be found in [15]. It is described to be able to best handle large problems and it satisfies bounds at all iterations and is furthermore able to recover from iterations when the function $f(s)$ returns an infinite or “Not a Number” value. The guide in [15] does not specify what exactly qualifies as a large problem compared to a small problem, but based on the complexity of the nonlinear single track model and the Extended Kalman Filter and the dimension of the input vector s it is assumed that the optimization problems in this thesis can be considered

“large”. Other algorithms provided by MATLAB[®] are either not recommended for large scale problems or require a gradient for the function $f(s)$.

Set Up for Tire Model

Initialization values for the optimization of the tire parameters are taken from [4] and shown in Table 3.

Table 3: Initial values and bounds for tire model identification

	B	C	D	k_{κ}	$k_{\mu x}$	k_{F_z}	F_{z0}
lb	10	1	0.5	1e-2	1e-2	1e-2	4000
s_0	15.09	1.51	1.19	0.88	1.30	0.17	5913
ub	25	2	2	2	2	2	10000

The lower bound lb and upper bound ub are chosen to set rough boundaries for the parameter space. According to [15] this can lead to faster conversion. It is assumed that through skillful selection of the dynamic maneuvers, the resulting tire model will automatically be physically plausible.

Set Up for EKF Parameter

After the parameters for the tire models for the front and rear axle are identified, the entries for the process noise covariance matrix Q are identified. The error, as defined in (3.2), is reduced by tuning the matrix Q . Start values for the gradient based optimization are chosen intuitively based on the expected magnitude of the state.

Table 4: Initial values and bounds of identification of Q

	Q_{x_1}	Q_{x_2}	Q_{x_3}	Q_{x_4}	Q_{x_5}
lb	0	0	0	0	0
s_0	1e-3	1e-3	1e-4	1e-4	1e-2
ub	1e2	1e2	1e2	1e2	1e2

Values < 0 are not plausible for the process noise covariance. The upper bounds are set high to allow for the possibility that the process noise covariance for a specific state can be chosen so high, that the estimate will basically be discarded by the EKF and only the measurement from the real vehicle is trusted.

Both Table 3 and Table 4 only show the initial set up. Based on [14], it is advisable to restart the *fmincon* function after the function returns a local minimum. The resulting values should be used as a new starting point with the bounds tightened around those values. This often leads to better results.

3.2 Error Definition for Gradient Based Optimization

The error that is to be reduced captures the states of the single-track model or the estimated states and compares them to the corresponding reference model over various maneuvers. The same error definition is used for finding the parameters for the tire model as well as the parameters of the EKF. The error e is defined as:

$$e = \sum_{m=1}^{N_m} \sum_{i=1}^{N_x} \frac{1}{n} \left(\sum_{k=1}^n (X_{k,i,m,\text{Single Track}} - x_{k,i,m,\text{Real Vehicle}}) \right)_i^2 \cdot \text{scaling}_i \quad (3.2)$$

which can be described as the squared sum of the difference of every state at every timestep, summed up over all states and maneuvers. The variable X is to be substituted with the states x of the single track model for the tire parameter identification or with the state estimate \hat{x} for the identification of the EKF parameters. N_m denotes the number of performed maneuvers, N_x the number of states, and n the number of timesteps performed in simulation. $x_{k,i,j,\text{Single Track}}$ is the value of state i of the state vector x of the single track model at timestep k of maneuver m . The same principle applies for the states of the real vehicle. The corresponding states of the real vehicle are taken as measurements from the simulation. These measurements coming from the simulation are noise free. If, instead of a simulated reference vehicle, a physical car is used, measurements would have to be post processed to remove sensor noise. A scaling factor is introduced and multiplied with the squared sum of each state, in an attempt to achieve equal influence of each state on the total error e , even if the specific state is generally of a higher magnitude. Each individual scaling factor is calculated with

$$\text{scaling}_i = \frac{1}{\max_{1 \leq m \leq N_m, 1 \leq k \leq n} (X_{k,i,m, \text{Real Vehicle}})^2} \quad (3.3)$$

The scaling factor is the inversed square of the maximal value the state i reaches in one of the maneuvers.

In Table 5, the scaling factor for each state is listed. They are the same for the identification of the tire model and the process noise covariance matrix.

Table 5: Scaling for tire parameter optimization

State variable	Scaling factor
$\dot{\psi}$	2.5674 s^2
v_x	$0.0011 \frac{\text{s}^2}{\text{m}^2}$
v_y	$0.6171 \frac{\text{s}^2}{\text{m}^2}$
a_x	$0.0356 \frac{\text{s}^4}{\text{m}^2}$

3.3 Maneuvers

The maneuvers that are performed with the real vehicle are crucial for the success of the identification of both the tire parameters and the matrix Q . It can be assumed, that the tire model is only valid within the regions of tire slip and normal load that are reached during the maneuvers. If the tires were to only be operated in their linear region during the maneuvers, the minimization function could choose a combination of parameters that govern the behavior in the nonlinear region without affecting the result of the evaluation of the error function (3.2) significantly. This would lead to a single-track model that would only be a good representation of the real vehicle in the linear region of tire excitation.

Furthermore, if there is no load transfer or longitudinal excitation during the maneuvers, the parameters of the tire model that govern these effects cannot be expected to be identified with high quality. Hence the maneuvers are chosen such that a high variability in the excitation of front and rear tire is achieved.

However, the identification of the driving resistance behavior has to be done first, since the driving resistance of the real vehicle should not influence the tire model of the single-track model.

3.3.1 *Coast-Down Test*

To identify the parameters d_1 , d_2 , and d_3 for capturing driving resistance as introduced in (2.7)-(2.9) a free rolling maneuver is performed. The real vehicle is accelerated to $30 \frac{m}{s}$ and then all wheel torque inputs are set to zero. The vehicle will gradually slow down through effects of air and rolling resistance. Only the deceleration is measured and used to tune the parameters d_1 , d_2 , and d_3 , such that the deceleration of the nonlinear single track model matches the deceleration of the real vehicle. The calculation of tire forces on the single-track model is disabled for this purpose.

The resulting parameters are shown in Table 6.

Table 6: Resistance parameters

Parameter	Value
d_1	76.57
d_2	4.15
d_3	0.38

3.3.2 *Dynamic Maneuvers*

The maneuvers are based on common maneuvers in vehicle handling testing and adjusted to meet the demands of the identification process. All three lateral maneuvers are used by [16] to determine tire parameters. The maneuvers are set to take 25s each and consist of an acceleration phase and a phase of the main excitation. The maneuvers are

- Quasi-Steady-State Circle
- Continuous Sine Wave
- Sine Wave with Increasing Frequency
- Emergency Braking

All maneuvers are performed twice, once on a high friction surface where the coefficient of friction is set to $\mu = 1$ and once on a low friction surface with $\mu = 0.4$. This is done to ensure that the parameters identified for the tire model are valid on different road surfaces and the estimation of the friction coefficient works for high and low friction surfaces. The speed at which the maneuvers are performed is reduced for the lower friction surfaces. A summary of the configurations of the maneuvers is shown in Table 7.

Quasi Steady State Circle

The maneuver is performed in order to capture the steady state behavior and the self-steering behavior of the vehicle. It is based on ISO 4138 (2004) and information taken from [17]. During the quasi-steady-state-Circle maneuver, the speed is kept constant and the steering angle of the wheels is steadily increased from 0° to 15° with a rate of $1.15^\circ/s$. The maximum steering angle is chosen based on trial and error, such that the vehicle

remains stable throughout the maneuver. This limit only applies for this specific vehicle and would have to be adjusted when performing the maneuver with a different vehicle. The goal is to reach high slip angles at the front and rear while sustaining stability and therefore repeatability. To sustain quasi-static conditions, an increase in the lateral acceleration of $0.2 \text{ m/s}^2/\text{s}$ must not be exceeded [18].

Continuous Sine Wave

To excite the vehicle and the tire in a repeated and consistent manner, a sine wave steering profile with constant frequency and amplitude is chosen. Once the desired speed is reached, the wheel steering angle is changed with a frequency of 0.25 Hz and an amplitude of 6.5° . The chosen frequency is the same as used in [16]. Vehicle speed and amplitude are chosen such that the vehicle reaches its lateral saturation. This is determined with test maneuvers and analyzation of the resulting yaw rate.

Sine Wave with Increasing Frequency (Sine Chirp)

To capture unsteady behavior of the real vehicle through different frequencies of excitation, a sine wave with increasing frequency is applied to the steering input. This is a maneuver to capture the frequency response of a vehicle. Based on ISO 7401 (2011) and according to [17] the steering wheel frequency is increased from 0.1 Hz to 3 Hz and the amplitude of the wheel steering angle is kept constant at 6.5° . The amplitude is based on trial and error and is limited by maintaining vehicle stability throughout the maneuver. This maneuver is usually performed with a steering robot, however, application in [16] shows that good results can be achieved with a human driver as well. This highly dynamic maneuver is performed to capture transient effects, which influence the lateral behavior of

the real vehicle. Here, things such as damping, roll inertia, and transient tire behavior come into play. Even though the observer model is not able to model those effects, it is desirable to find an observer model that displays a compromise between steady state as well as highly dynamic conditions.

The input profile is shown in Figure 7. Note that this is the steering angle at the wheels, not the steering wheel. To replicate these maneuvers on a different vehicle, the steering ratio between steering wheel and wheels has to be taken into consideration.

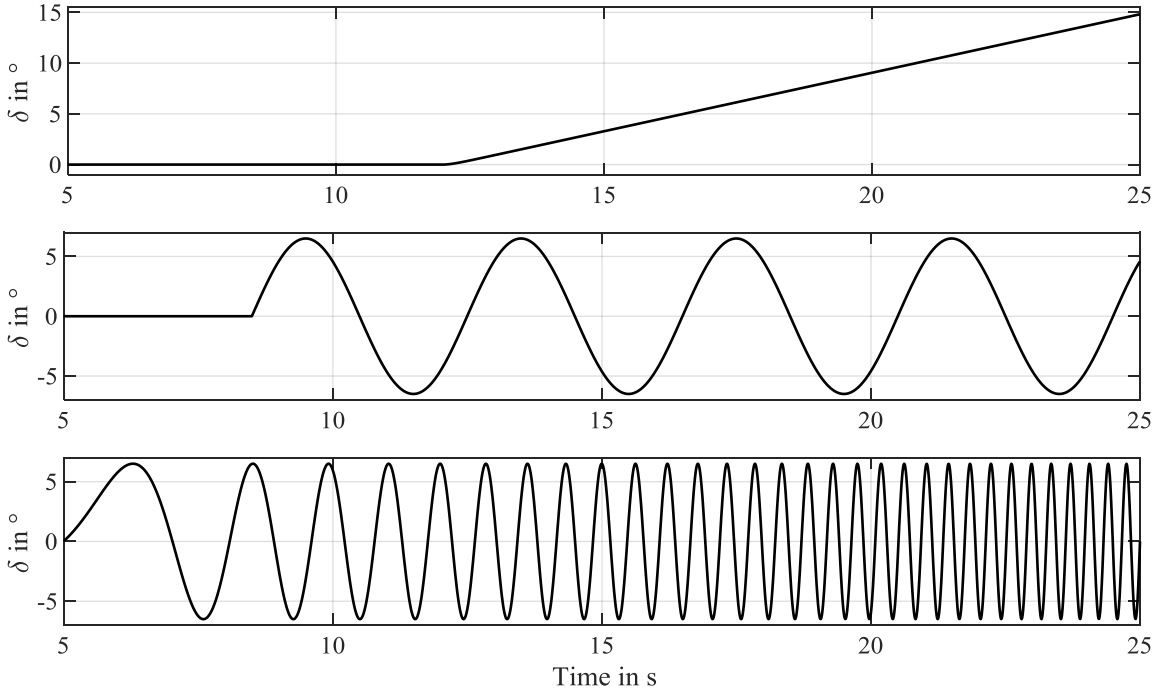


Figure 7: Steering input profile dynamic maneuvers

The configuration for the steering maneuvers, for the different surfaces are shown in Table 7.

Table 7: Overview parameters lateral maneuver

Maneuver	Speed on		Max δ	Steering rate
	$\mu = 1$	$\mu = 0.4$		
Quasi-Steady-State-Circle	100 $\frac{km}{h}$	40 $\frac{km}{h}$	15°	1.15 $\frac{^\circ}{s}$
Continuous Sine Wave	100 $\frac{km}{h}$	60 $\frac{km}{h}$	6.5°	0.25 Hz
Sine Wave with Increasing Frequency	80 $\frac{km}{h}$	30 $\frac{km}{h}$	6.5°	0.1 Hz – 3 Hz

The maximal reached slip angle for each maneuver at front and rear are listed in Table 8.

These also represent the limited region within the tire model that is assumed to be valid.

Table 8: Maximal reached slip angle during dynamic maneuvers

Maneuver	$\mu = 1$		$\mu = 0.4$	
	$ a_{F,max} $	$ a_{R,max} $	$ a_{F,max} $	$ a_{R,max} $
Quasi-Steady-State-Circle	0.2702	0.0465	0.2136	0.0188
Continuous Sine Wave	0.1430	0.0624	0.1018	0.0204
Sine Wave with Increasing Frequency	0.1175	0.0754	0.1053	0.0144

Emergency Braking

To reach high excitation in longitudinal direction and generate a load transfer, such that the tires are operated under various loads, an emergency braking event is performed.

Furthermore, none of the mostly lateral maneuvers lead to a high lateral or longitudinal slip at the rear tire. A longitudinal excitation is needed to determine the parameters of the tire model that govern the longitudinal behavior. Emergency braking is used to describe that a very high braking pressure is applied and the anti-lock braking logic is activated. It is expected, that the anti-lock braking system leads to operation of the tire in the nonlinear region. The unsteady nature of a such a braking maneuver leads to high variability in the achieved longitudinal slip, compared to braking with locked wheels. Furthermore, it is assumed that a vehicle that is supposed to be equipped with a tire-road friction estimator is already equipped with an anti-lock braking system as it is one of the most common safety systems. This makes emergency braking the easiest way to reach high longitudinal excitations for the purpose of tire parameter identification. The achieved acceleration profile during the maneuver is shown in Figure 8.

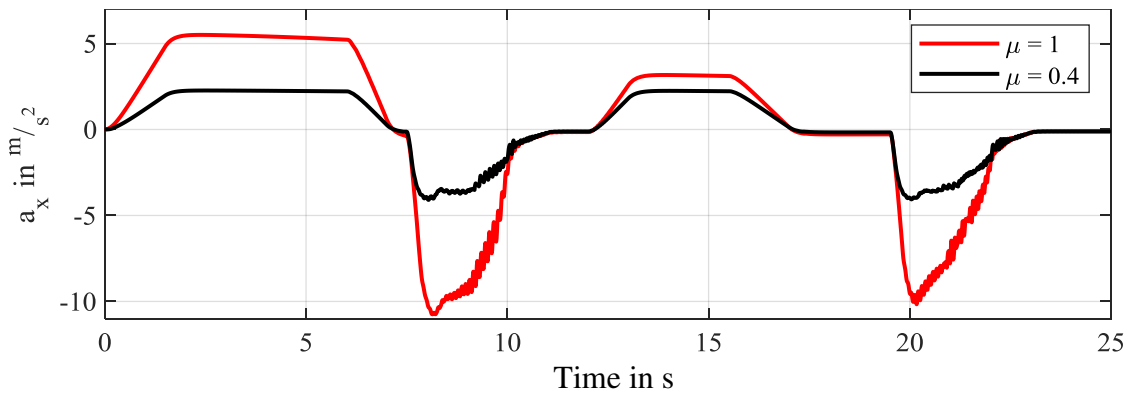


Figure 8: Acceleration profile for emergency braking

For this vehicle this leads to maximal slip values as shown in Table 9.

Table 9: Max longitudinal slip values for emergency braking

Maneuver	$\mu = 1$		$\mu = 0.4$	
	$\kappa_{F,max}$	$\kappa_{R,max}$	$\kappa_{F,max}$	$\kappa_{R,max}$
Emergency Braking	0.18	0.2	0.28	0.3

Just as the achieved slip angle during the lateral maneuvers depends on the dynamic characteristics of the vehicle and the kinematics of each axle, the achieved longitudinal slip is specific to the vehicle the maneuver is performed with. This is tolerable, as the tire model only needs to be valid for the limit of vehicle dynamics of the specific vehicle.

4 RESULTS

The results of the identification process are presented and discussed in the following chapter. First, the results for the tire identification are shown, as well as the plots for the resulting tire models. Afterwards, the results for the identification of the process noise covariance matrix Q are discussed. The chapter concludes with showing the results of verification maneuvers where the friction coefficient is estimated during various, somewhat arbitrary, maneuvers. Only selected maneuvers are displayed in this chapter, all results can be found in the Appendix.

4.1 Tire Identification

The parameters for the tire model that are returned by the *fmincon* function are applied to the single-track model and the maneuvers are performed again. The results for the identification on $\mu = 1$ are shown and discussed. The graphs for the maneuvers performed on $\mu = 0.4$ can be found in the appendix. Even though the optimization is done by comparing all states of the single-track model to the reference measurement of the real vehicle, for easier readability only the most relevant states for each maneuver are plotted.

The results for the semi-steady-state circle maneuver are shown in Figure 9.

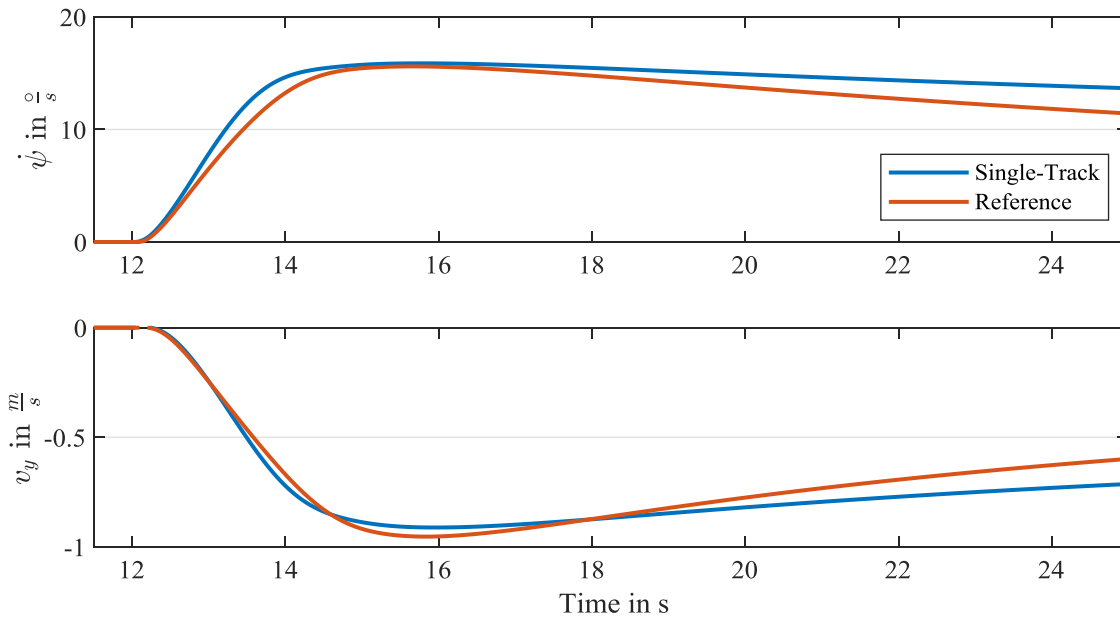


Figure 9: Result of tire identification for semi-steady-state circle on $\mu = 1$

The yaw rate $\dot{\psi}$ and the lateral velocity v_y reach their peak value at around 15s when the steering angle has reached a value of roughly 3.7° (compare with plot of steering angle, Figure 7). This means that the tires at the front have reached their maximum and there is no further increase of transmittable force for an increasing sideslip angle. It can be observed, that the single-track model is not able to capture these effects perfectly for a semi-steady-state case. Note that the steering angle and the slip angle reached for this maneuver are much higher than for other maneuvers (see Table 7). The next maneuver is the constant sine wave maneuver. The result of the identification is shown in Figure 10. The single-track model replicates the behavior of the reference vehicle almost perfectly.

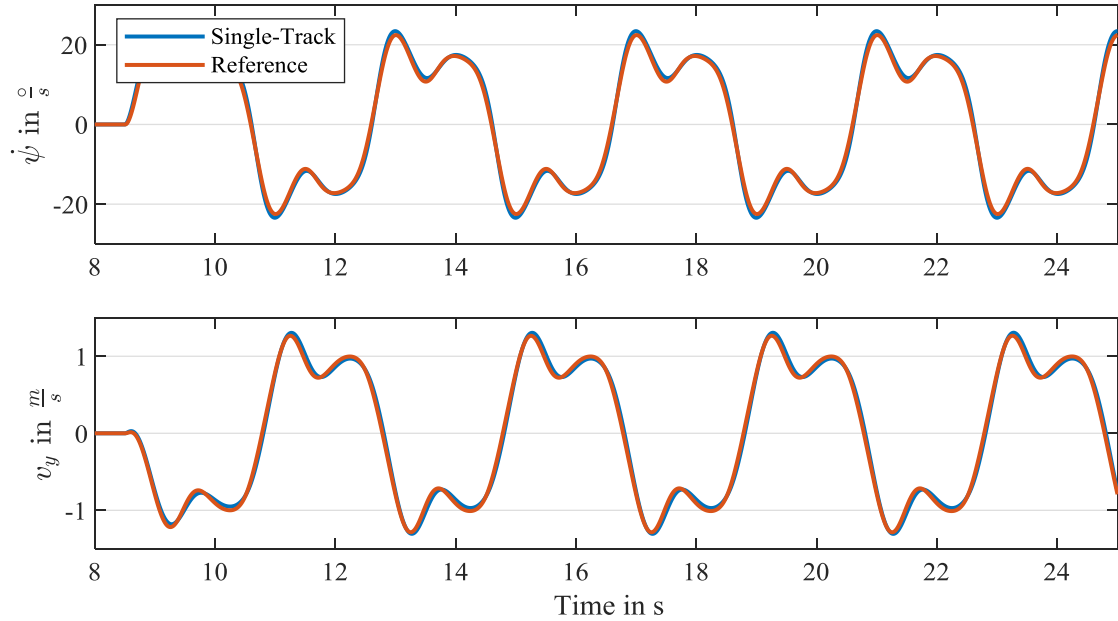


Figure 10: Result of tire identification for constant sine wave on $\mu = 1$

Display of the result of the sine chirp maneuver is omitted for brevity, as the fit shows no visual discrepancy. Results can be found in the appendix. The behavior for the purely longitudinal maneuver is shown in Figure 11. Comparing the two plots, the single-track model does not seem to be able to capture the behavior of the real vehicle very well.

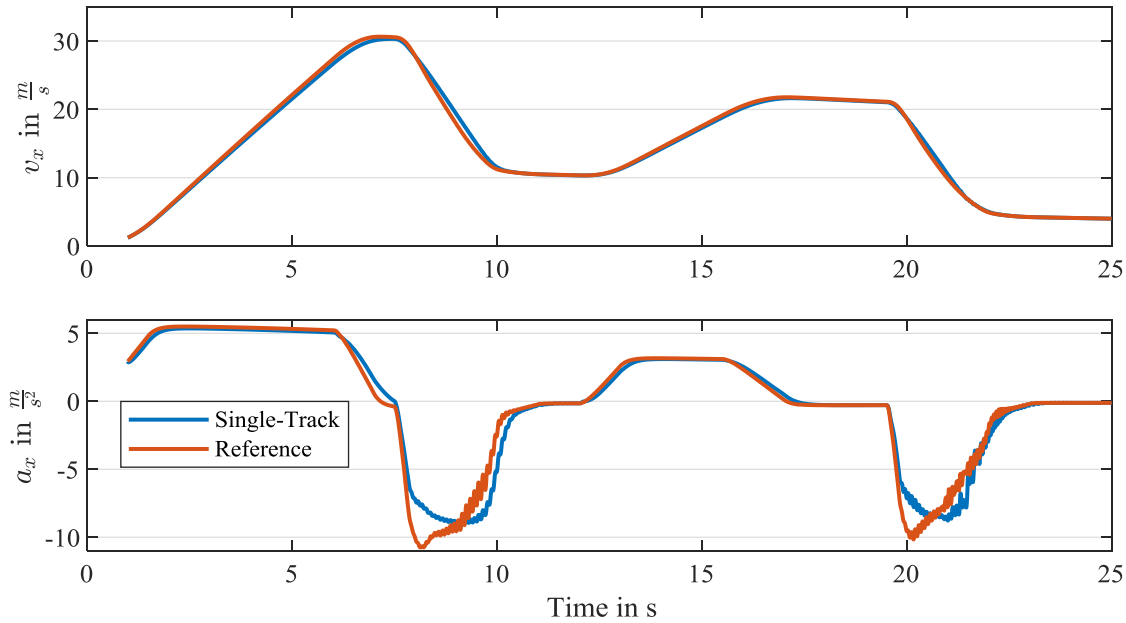


Figure 11: Result of tire identification for braking maneuver on $\mu = 1$

The cause for this discrepancy lays in the problems with the normal force modeling as described in Chapter 4.1.1. The quality of the results is lower for the maneuvers performed on a low friction surface with $\mu = 0.4$. Note that the identification process has been done with all 8 maneuvers together at the same time, so it can be speculated that the incorporation of the friction coefficient into the tire model as done in equations (2.15) to (2.20) might not be an ideal representation for low friction regions.

The resulting tire model for the front axle is shown in Figure 12 and Figure 13. The first figure shows the influence of the applied normal force on the tire behavior with $\mu = 1$. The second figure shows the influence of changing μ .

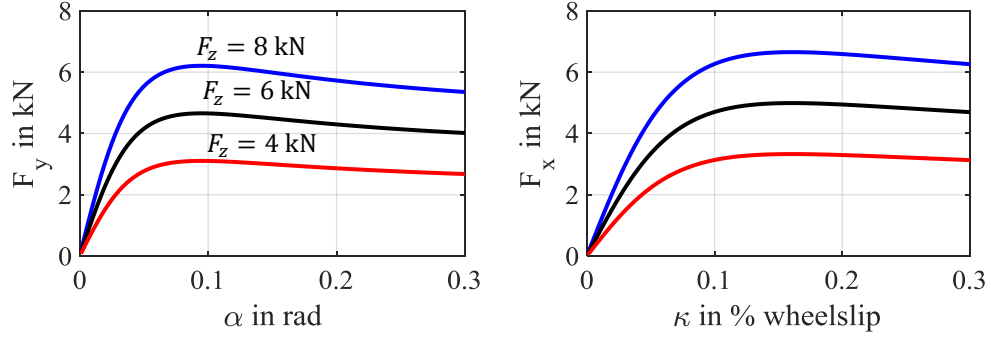


Figure 12: Influence of normal force on front axle behavior with $F_z = 8 \text{ kN}, 6 \text{ kN}, 4 \text{ kN}$ on $\mu = 1$

At a normal force of 8000 N, the front axle is only able to transfer a side force of 6000 N. Furthermore, the tire shows a lower stiffness in longitudinal direction than in lateral. This is unusual, as vehicle tires, due to their construction almost always have a higher stiffness in the longitudinal direction [10]. For completeness, the influence of different μ on the tire behavior is shown in Figure 13.

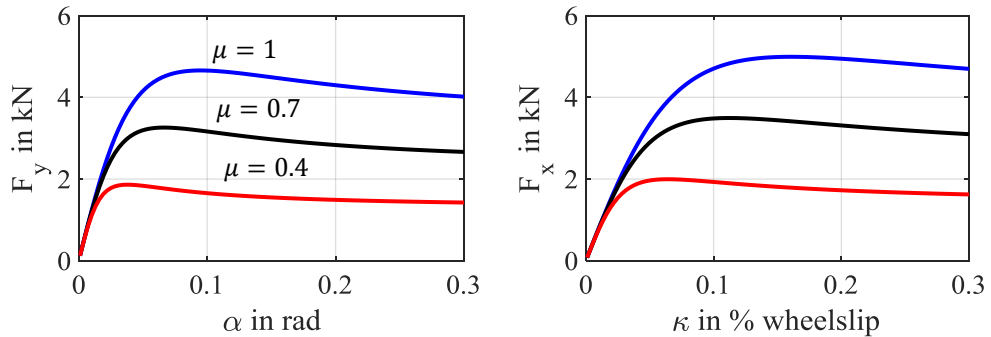


Figure 13: Influence of change in μ on front axle behavior on $\mu = 1, 0.7, 0.4$ with $F_z = 6 \text{ kN}$

The tire model for the rear axle is shown in Figure 14 and Figure 15. By comparing the height of the peak values for different normal loads it can be observed that the rear axle is significantly stiffer than the front axle in the longitudinal as well as in the lateral directions.

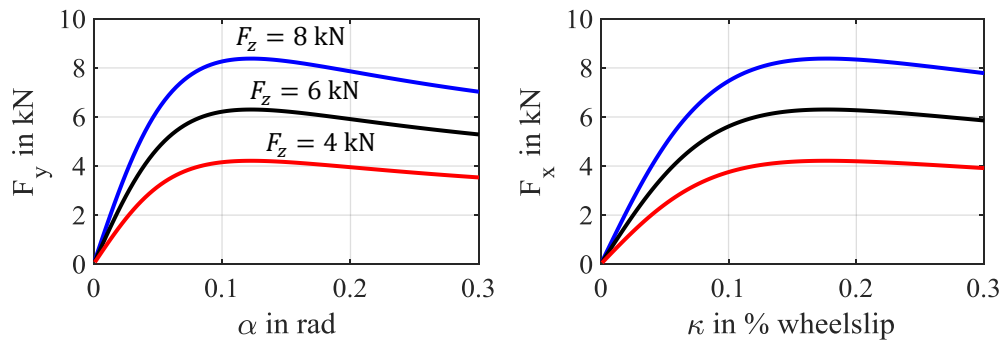


Figure 14: Influence of normal force on rear axle behavior with $F_z = 8$ kN, 6 kN, 4 kN on $\mu = 1$

For completeness, the influence of different μ on the tire behavior is shown in Figure 15.

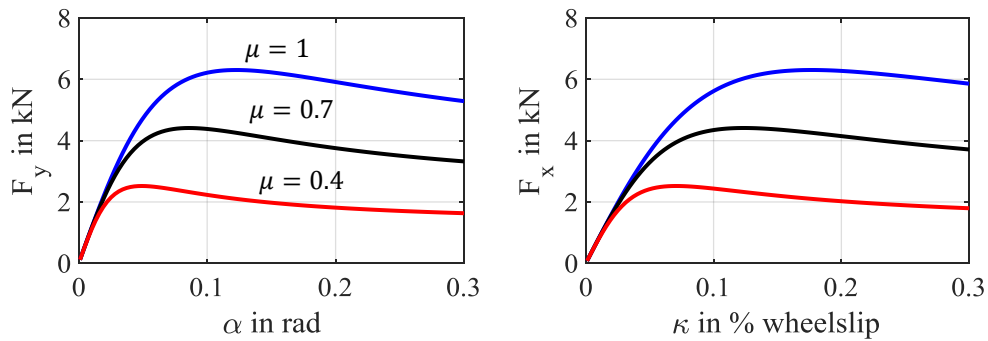


Figure 15: Influence of change in μ on rear axle behavior on $\mu = 1, 0.7, 0.4$ with $F_z = 6$ kN

The resulting parameters for the tire model for the front and rear are shown in Table 10.

Table 10: Resulting tire parameters front and rear

	B	C	D	k_κ	$k_{\mu x}$	k_{F_z}	F_{z0}
Front	17.78	1.52	0.78	0.59	1.07	0.0013	8683
Rear	11.06	1.68	1.05	0.69	1.00	0.0125	8441

As mentioned in Chapter 2.2.2, each tire model of the single-track model has to represent the behavior of the complete axle of the real vehicle. Figure 16 shows the resulting lateral tire forces for the constant sine wave maneuver for a segment between 8s and 9s. The forces

of the single-track model align well with the forces of the real vehicle. This is to be expected as otherwise the vehicle motion would not closely match as shown in Figure 10. One can observe that the rear axle (plot b)) has a higher lateral stiffness than the front axle. This is to be expected as the front suspension of the real vehicle is an independent suspension with steering and the rear suspension is a solid axle. This leads to a difference in compliance under lateral force, and the solid axle is seemingly stiffer than the front suspension.

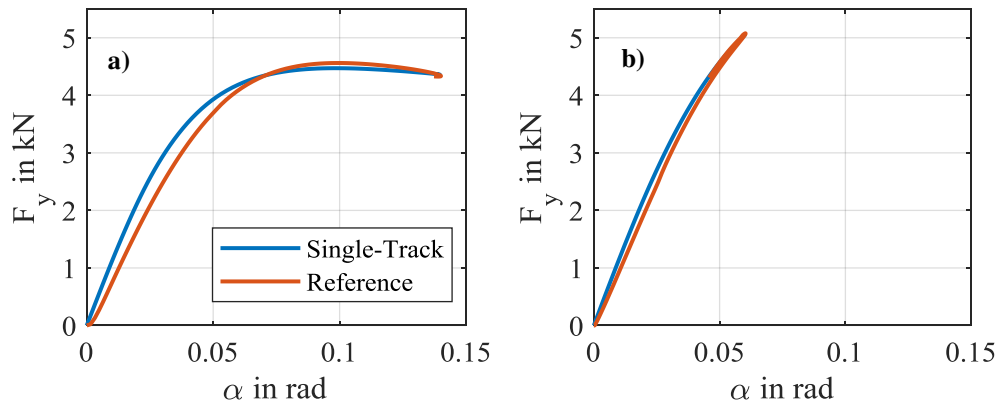


Figure 16: Lateral tire forces during sine wave maneuver between 8s-9s with a) front tire and b) rear tire

However, the situation is completely different when the normalized axle forces are compared. Figure 17 shows the normalized axle forces for the same maneuver. Here, a stark difference between the single-track model and the reference vehicle is visible, especially on the rear axle.

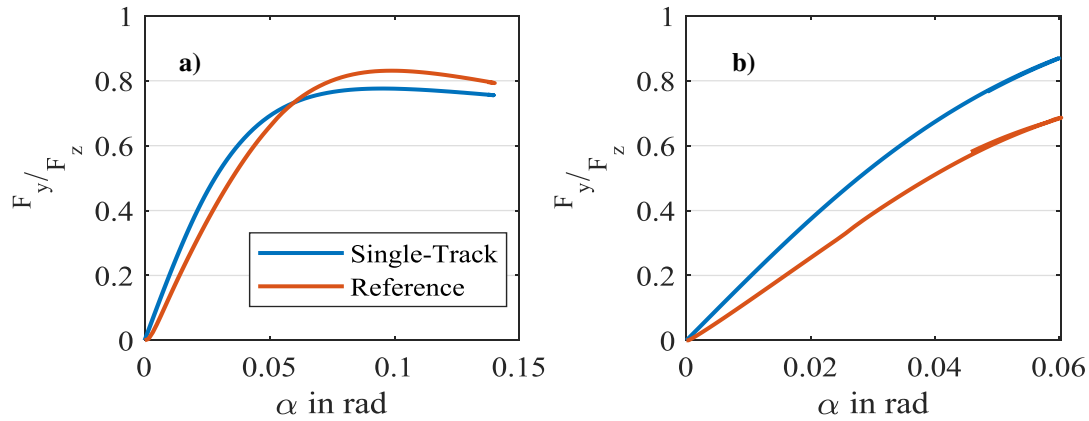


Figure 17: Normalized lateral tire forces during sine wave maneuver between 8s-9s with a) front tire and b) rear tire

Where this discrepancy comes from and the resulting problem are explained in the next chapter.

4.1.1 *Inconsistency within the Reference Vehicle Model*

While working with the MATLAB/SIMULINK[®] vehicle model, some problems occurred that influenced the quality of the work. In order to set up the simplified vehicle dynamic model, the basic geometric and mass properties of the reference model are retrieved from the model configuration file. They are shown in Table 1. With this position of the center of gravity, the vehicle has a static weight distribution of 51% on the rear and 49% on the front axle. With the weight of the vehicle of 1181 kg, this would lead to a total static normal force on the front axle of 5708 N and 5877 N on the rear axle. The simulation setup allows for easy display of the normal forces on each wheel. Analyzing the normal forces of the standing vehicle shows a total normal load on the front axle of 5760 N and a normal load on the rear axle of 7394 N. This would mean a total vehicle weight of 1340 kg and a normal force distribution of 55/45. Since the analysis is done for the standing vehicle

as well for low speeds, an aerodynamic influence can be excluded. Now, one could conclude that the information given in the model configuration must be incomplete and might be limited to the vehicle body, but excludes additional weight, like passengers or luggage that might be part of the simulation. However, further analysis of the vehicle model was conducted by comparing the sum of the lateral forces to the lateral acceleration, which revealed that the vehicle body mass is indeed 1181 kg. Comparing applied lateral forces with the resulting yaw rate of the vehicle shows a position of the center of gravity of 51/49 rear to front, so the normal force distribution of the tires is different and unrelated to the vehicle mass and position of the center of gravity. The normal force on the front and rear axle for the real vehicle and the single-track model is shown in Figure 18. The normal forces are recorded for the constant sine wave maneuver. The slight decrease in normal force on the front axle and vice versa, the slight increase in normal force on the rear axle, is due to aerodynamic effects. The rear axle of the real car shows a normal force that has a constant offset of 1510 N compared to the single-track model.

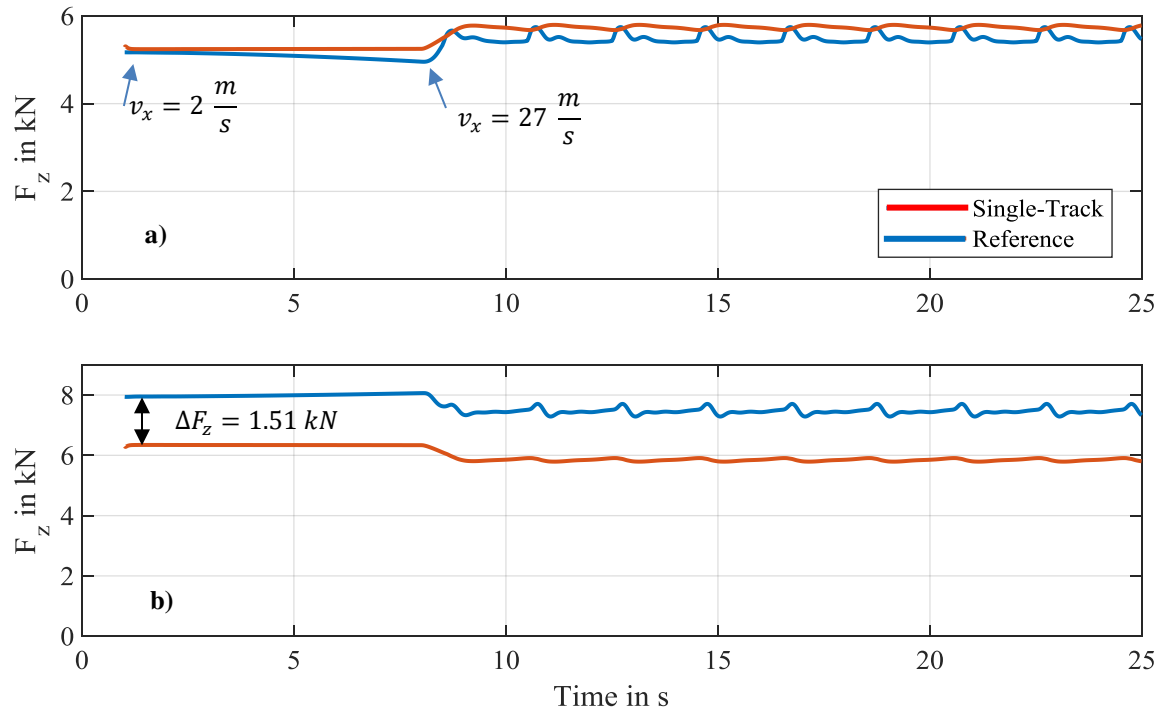


Figure 18: Normal force on a) front axle and b) rear axle for real vehicle and single-track model during sine wave maneuver

That it is in fact not an error in modeling of vehicle mass and position of center of gravity can easily be proven by comparing the lateral forces acting during the maneuver. They are shown in Figure 19.

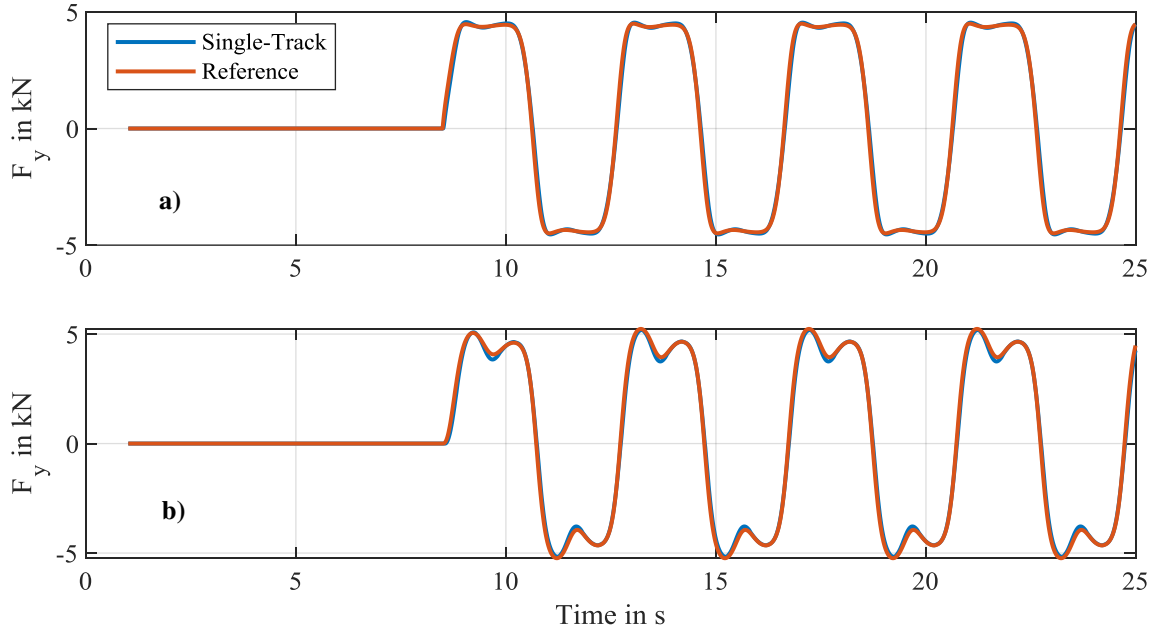


Figure 19: Lateral forces on a) front and b) rear axle during constant sine wave maneuver

As the lateral forces on front and rear axle very closely match between the reference vehicle and the single-track model, it can be concluded that the mass of both vehicles must be the same and the position of center of gravity is identical. Unfortunately, the source of the additional constant normal force on the rear axle of the reference vehicle could not be identified and not eliminated.

4.2 EKF Parameter Identification

The result of the identification of the process noise covariance matrix are shown and discussed. Again, only some of the performed maneuvers are displayed here and the rest can be found in the Appendix. For all graphs in this subchapter, the black line represents the reference and noise free measurement, the blue line is the measurement that is taken from the real vehicle, and the red line is the estimated state. For all maneuvers, μ is initialized 0.2 below the actual value. Results for the estimation of μ during the semi-steady-state circle on $\mu = 1$ are shown in Figure 20. The estimation of μ during this

maneuver shows unsatisfactory results. During the early phase of the maneuver, where the vehicle accelerates, the estimation of μ starts to develop towards the real value of $\mu = 1$, but does not actually converge on it. During the phase of lateral acceleration, the estimation of μ does not converge on the real value either, but shows a tendency to be estimated too low. However, the estimation of $\dot{\psi}$ and v_y are very good. The error compared to the simulation without EKF is reduced, as a visual comparison with Figure 9 shows. This is also most likely the reason for the unsatisfactory result of the estimation of μ . When analyzing Figure 9, the error of $\dot{\psi}$ and v_y increases, as the steering angle is increased over the course of the maneuver. Both of those states are calculated to be of a higher magnitude in the single-track model, compared to the reference measurement. It is assumed, as a result of that, that the EKF estimates μ continuously lower than the actual μ , as this would lead to a reduction in $\dot{\psi}$ and v_y and thereby reduce the overall error.

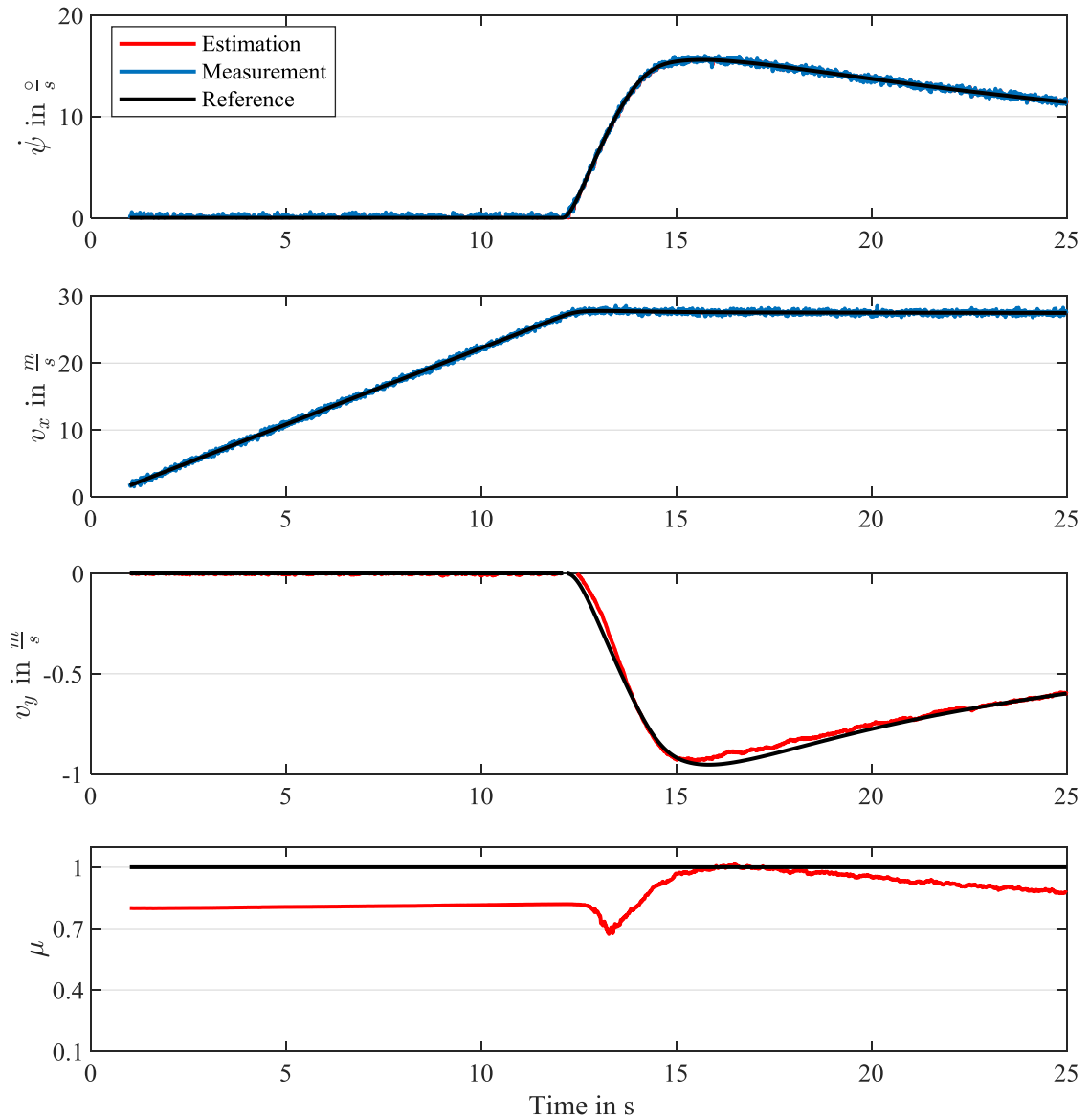


Figure 20: Result of μ estimation for steady-state-circle on $\mu = 1$

Results for μ estimation during the constant sine wave maneuver are displayed in Figure 21. Throughout the maneuver, the estimation of μ stays close the real value. During the phase of low excitation, while the vehicle accelerates, the estimated μ converges slowly

towards the real value. The short dip right when the lateral excitation starts can be observed throughout all maneuvers. It remains unknown why this is the case.

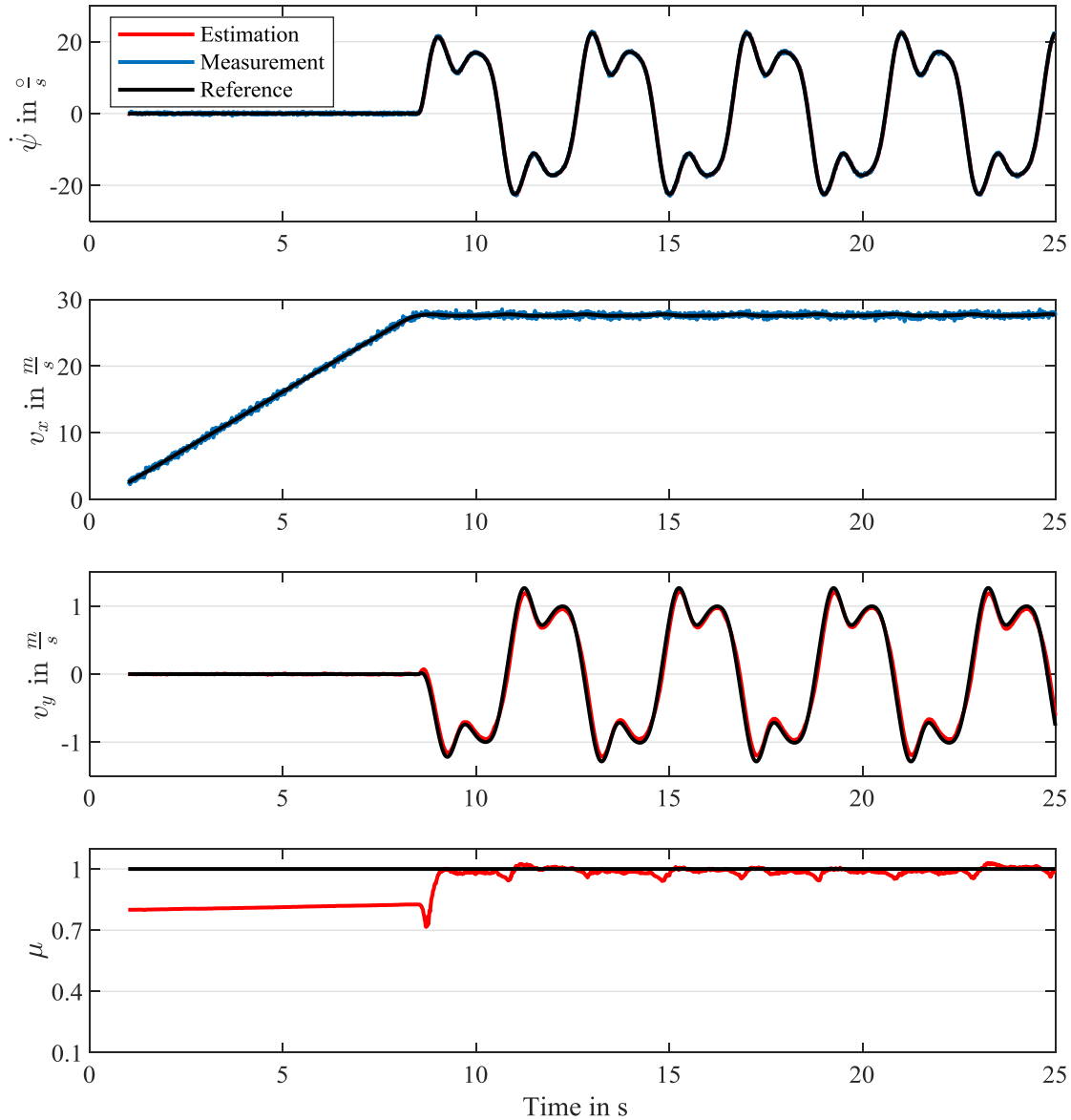


Figure 21: Result of μ estimation for constant sine wave maneuver on $\mu = 1$

As the single-track model matches the behavior of the real vehicle very well during this maneuver, the estimation of μ yields good results. The braking maneuver is shown in Figure 22. The estimation of μ slowly converges to the real value during the initial acceleration phase. During the deceleration, μ changes more dynamically and stays around

the real value of μ . It is noticeable that during phases of constant velocity, in other words, very low tire excitation, the estimated value of μ does not change much. During the second braking maneuver, the estimation of μ overshoots the real value. A plausible explanation is that the single-track model does not reach the deceleration of the real vehicle (Figure 11) and the friction coefficient is estimated too high, as this would increase the braking performance of the single-track model. Furthermore, the estimated value of a_x completely matches the measurement taken from the vehicle.

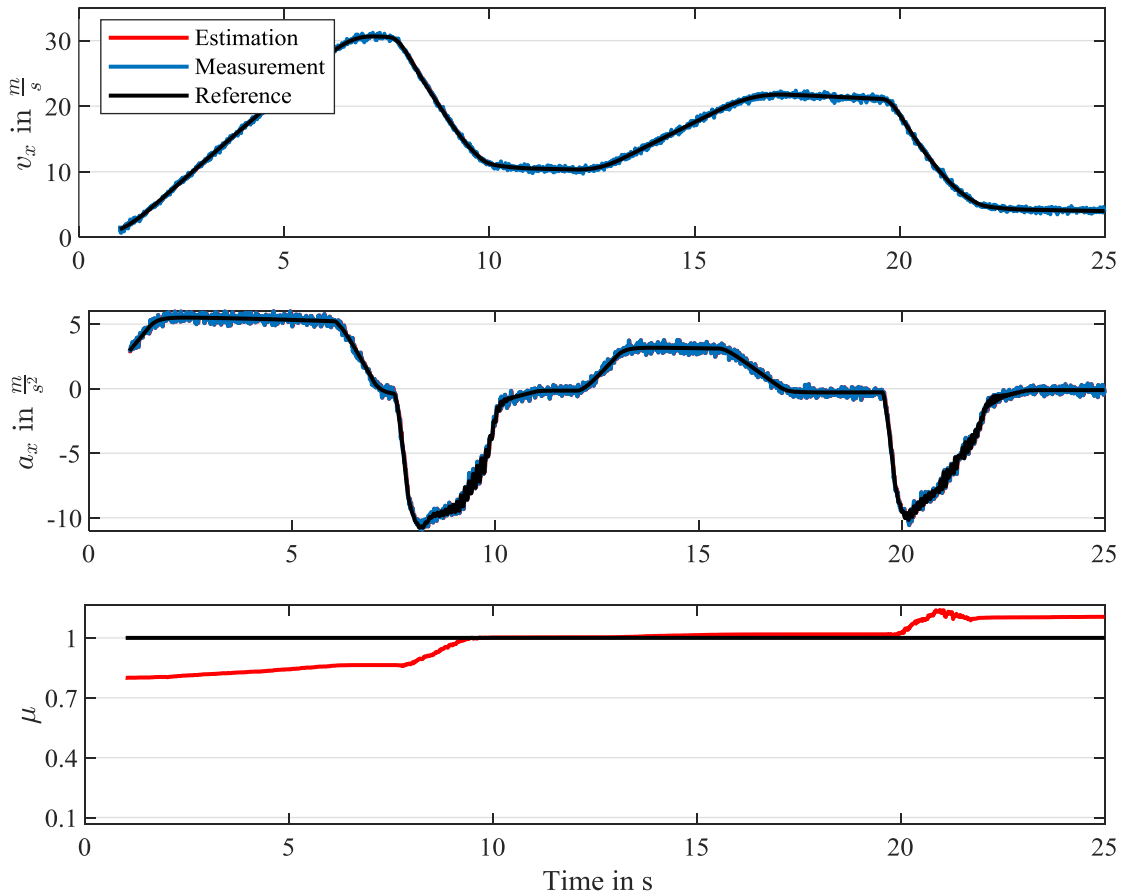


Figure 22: Result of μ estimation for braking maneuver on $\mu = 1$

The resulting values for the process noise covariance matrix are shown in (4.1). Due to the single track model's inability to represent the longitudinal dynamics of the reference

vehicle very well, the identification process for the process noise covariance matrix yields a very high value for the process noise covariance of the longitudinal acceleration a_x . In a practical sense this means that the estimated value \hat{a}_x is basically discarded and only the measurement coming from the real vehicle is trusted.

$$\text{diag}(Q)=[2.5665e-5 \quad 8e-3 \quad 1.355e-5 \quad 1e3 \quad 6.85e-6] \quad (4.1)$$

4.3 Verification

In order to verify the performance of the observer model and tire-road friction coefficient observer, some new maneuvers are performed with varying friction. They are intended to roughly resemble situations that could occur in real life driving situations.

The first test is a maneuver with increasing steering angle on a decreasing friction surface. The wheel steering angle is shown in Figure 23. The maneuver is performed with constant velocity.

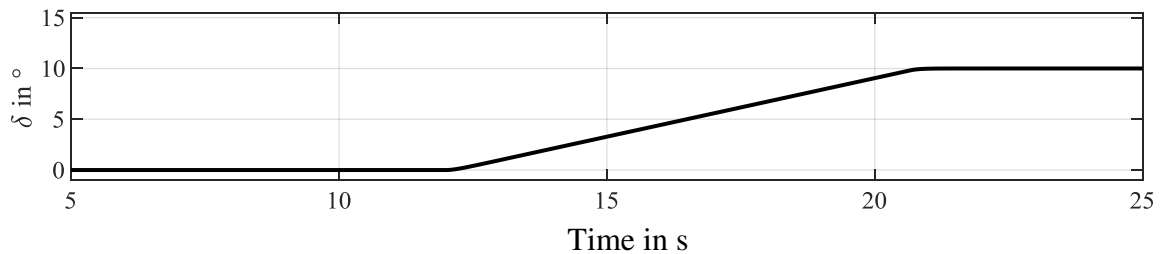


Figure 23: Steering angle first verification maneuver

The results are shown in Figure 24. While the estimation of μ shows the correct trend, there are some shortcomings in the estimation. The estimated μ does not converge towards the real value and the estimation moves towards the real value, only when there is enough excitation. The estimated value of μ starts visibly changing at around 15s into the

maneuver. This is most likely because the tire behavior for very low side-slip angles is identical for different μ , so the observer is unable to identify μ until the excitation is high enough.

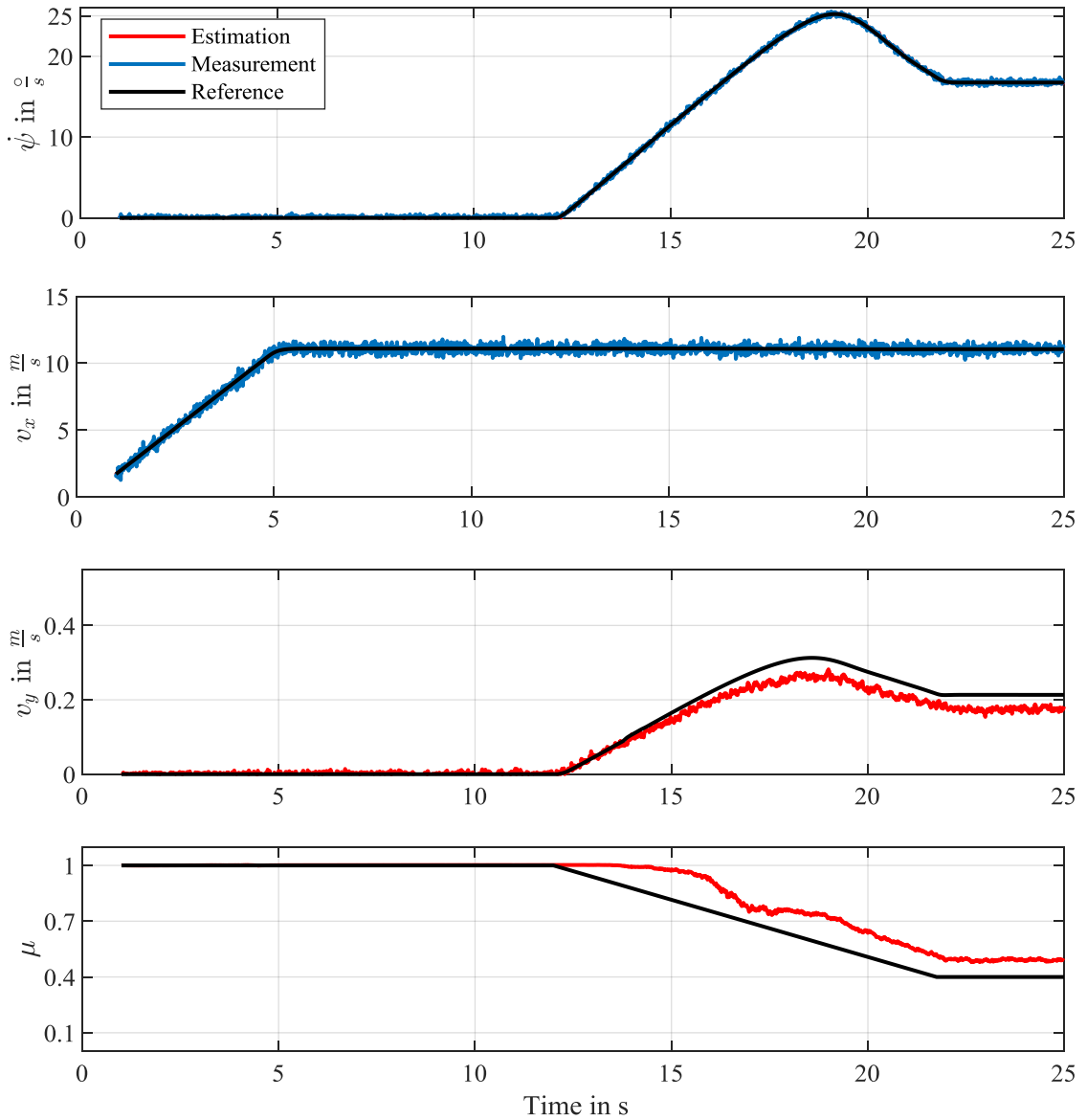


Figure 24: Result estimation process first validation maneuver

The second maneuver for validation is a succession of quick steering excitations on a surface where the coefficient of friction changes in sudden jumps.

The wheel steering angle profile is shown in Figure 25.

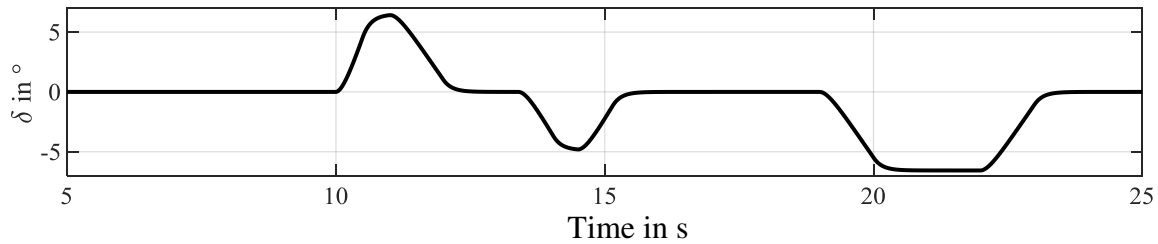


Figure 25: Steering profile for second verification maneuver

The results are shown in Figure 26. Except for a quick diverging of the estimated μ when the first steering excitation starts, the estimation of μ shows the same behavior as in the first validation maneuver. The first dip, just after 10s into the maneuver can also be observed in the maneuvers of Chapter 4.2. The reason for this is unknown. Apart from that, the estimation shows good tracking as long as the excitation of the tire is high enough. While the vehicle drives straight, the estimation of μ remains on the last known value even if μ abruptly changes. Since a sudden change of μ has no effect on the dynamic behavior of the vehicle during a drive on a straight line with constant velocity, it cannot be observed. When the second steering sweep is performed, at around 13.5s to 16s, the estimation of μ reacts quickly, but settles with a constant error from the true value. During the third steering excitation between 19s and 23.5s, the estimation again shows a quick reaction to the change in μ .

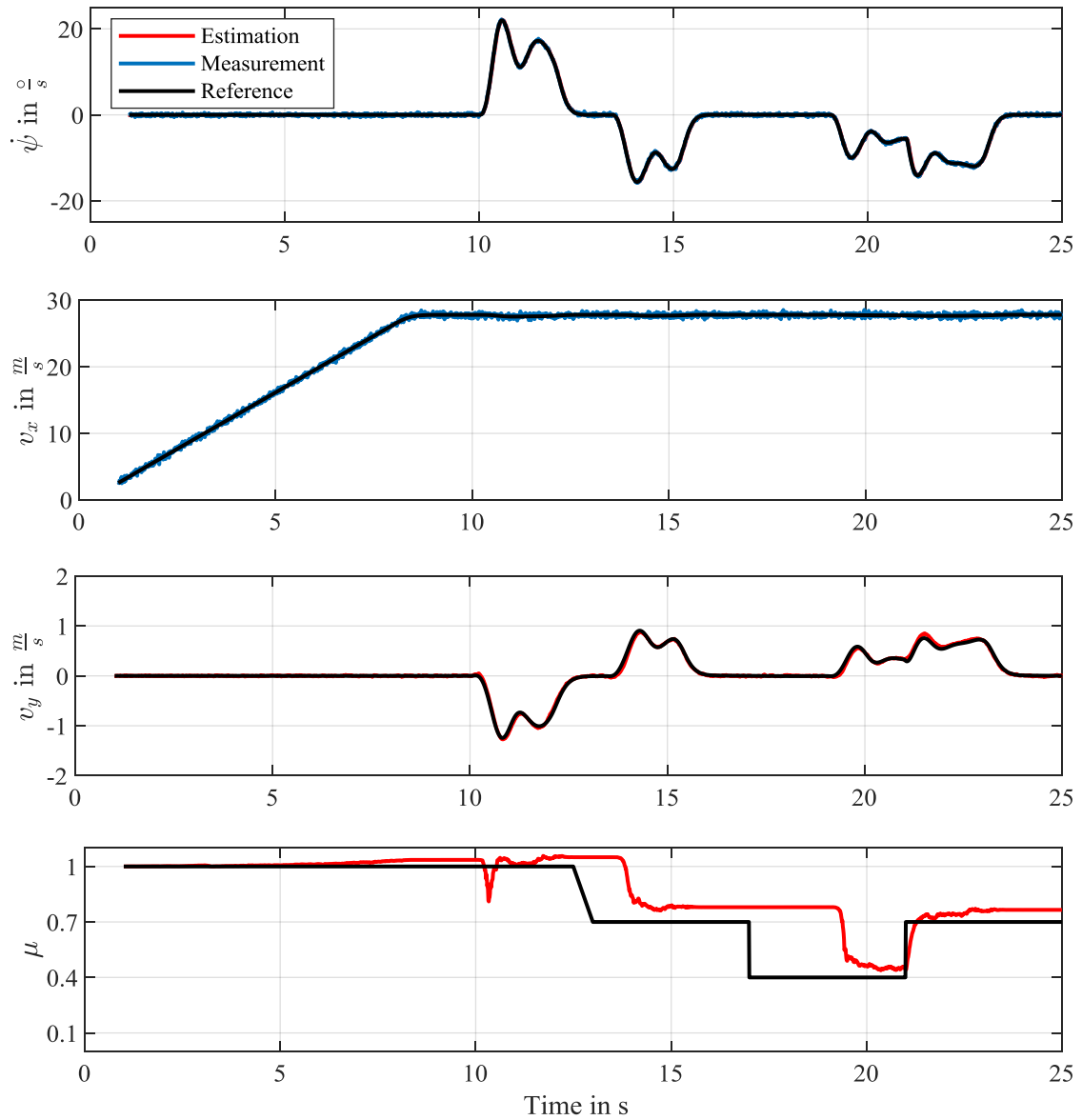


Figure 26: Result estimation process second validation maneuver

4.3.1 *Justification for Maneuver Choice*

In order to show the necessity of having a broad spectrum of maneuvers on different surfaces, a quick justification is done by showing the results of the identification if the maneuvers are only performed on the high friction surface. In this example, the identification of the tire parameters and the noise covariance matrix are done only with the maneuvers where $\mu = 1$. Afterwards, the identification of μ is carried out for all maneuvers. While the quality of the results for the maneuvers on $\mu = 1$ remains comparable, Figure 27 shows the performance of the friction estimation on $\mu = 0.4$. Even though Table 8 shows that the maximal sideslip angles for the sine sweep maneuver are higher for the $\mu = 1$ maneuver than the $\mu = 0.4$ maneuver, the results clearly show the necessity to perform the identification maneuvers on surfaces with different friction levels..

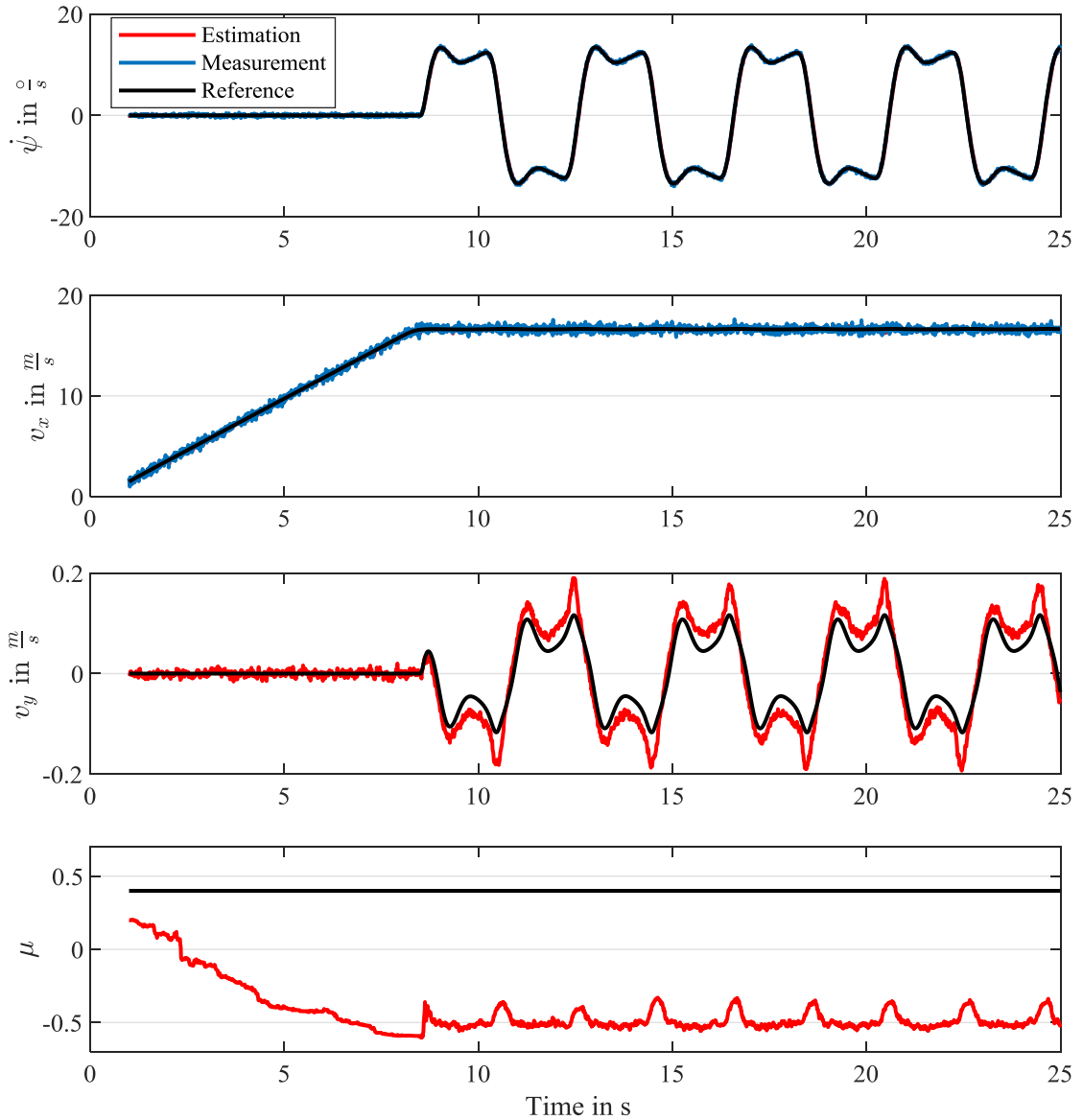


Figure 27: Performance of μ estimation on $\mu = 0.4$ when identification is only done on high friction surface.

A similar test is conducted by performing the identification maneuvers while reducing the speed described in Table 7 to half of its previous value. This reduces the expected slip angle that is reached for all maneuvers. After identifying the tire and EKF parameters with these changed maneuvers, the original maneuvers are performed again. The results for the sine chirp maneuver (original configuration) are shown in Figure 28.

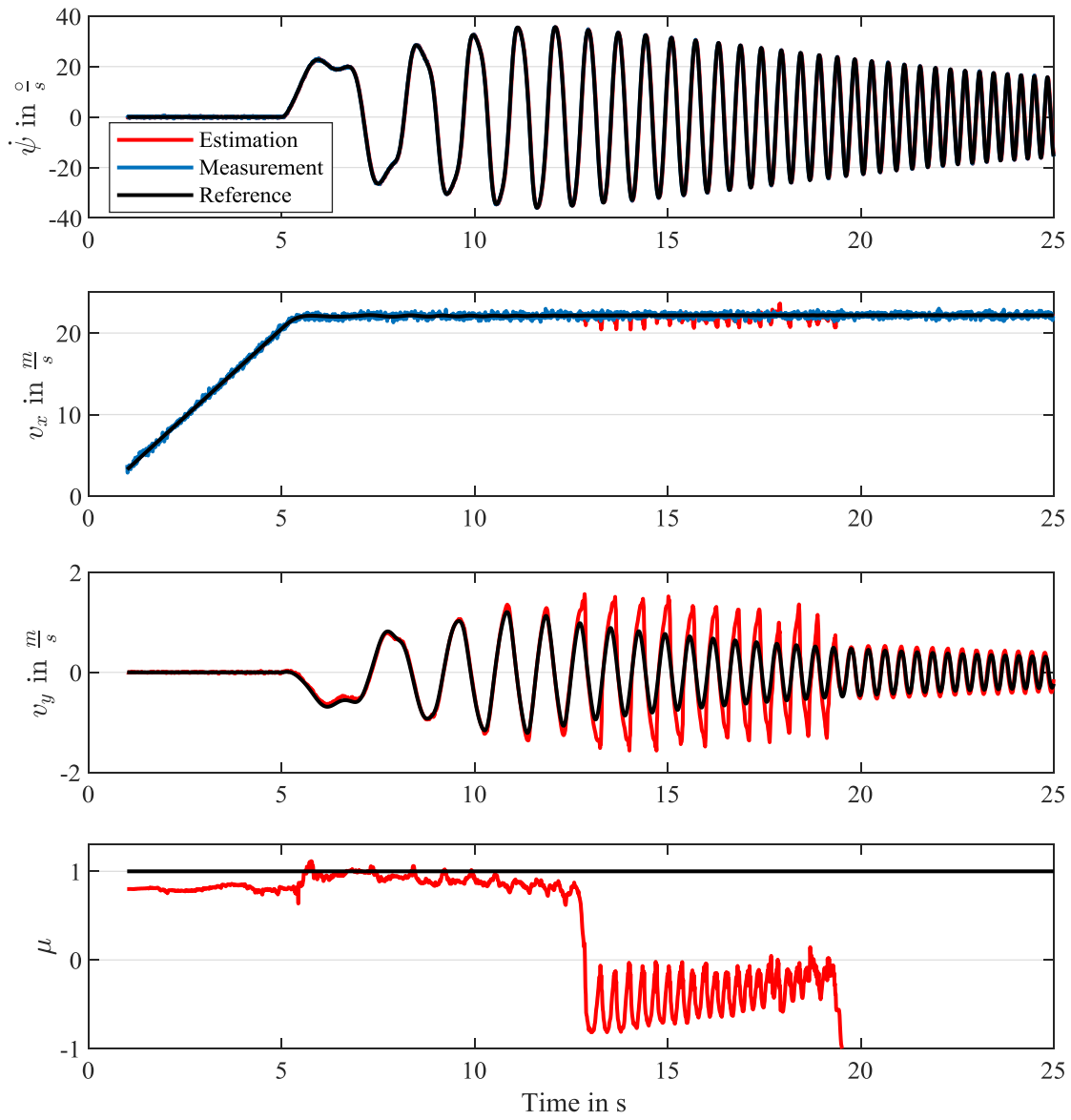


Figure 28: Performance of estimating μ during original maneuver, when identification of tire and EKF is done with maneuvers with reduced speed

5 CONCLUSIONS

In order to estimate the tire-road friction potential during highly dynamic driving operations a tire-road friction observer was developed. The observer used was an Extended Kalman filter that uses a nonlinear single-track model as the observer model. Dynamic maneuvers were set up to identify the tire parameters of the single-track model and the EKF by solving a minimization problem.

It can be concluded, that the tire model identified through dynamic maneuvers and measurements with standard sensors is suitable to be used as part of the observer model for a tire-road friction observer. To validate the resulting observer, maneuvers on different friction potentials were performed. Given sufficient excitation of the tires, the observer quickly identifies the current friction potential. The problem of needing a sufficient excitation to correctly estimate the current friction potential is inherent to the observer design. The tire behavior for different surfaces does not differ for very low slip regions. This does not necessarily limit the practical use of the designed friction observer, as knowledge about the friction potential is most useful when the tire is at risk to operate at the limit of its potential. However, a limitation to the finding is, that the identification of the tire model and the EKF parameters was done in an ideal simulation environment with noise free reference data for tuning. Furthermore, exact knowledge of the friction coefficient for tuning was assumed at all times.

During development of the maneuvers, the quality of the tire parameter identification has proven to be the crucial factor for the overall quality of the resulting observer. This leads to suggesting for future research to focus on maneuver design and the design of the

observer model. The observer model should be extended to a two-track model to capture load transfer under lateral acceleration. Initial tests with a two track model (rigid suspension), that, due to time limitations, have not made it into the final draft of this work showed great improvement in the accuracy and speed of the friction potential estimation. Furthermore, a maneuver should be added that includes combined slip cases such as braking or accelerating during cornering. Further suggestions aim towards the parameters of the tire model. A sensitivity analysis should be done to determine which parameter influences which characteristics of the tire the most. This could be used to determine the scaling on different maneuvers and states or exclude certain parameters from the identification process and fix them beforehand based on literature research.

APPENDIX

The Appendix shows the results for all identification maneuvers.

A.1 All Results Tire Identification

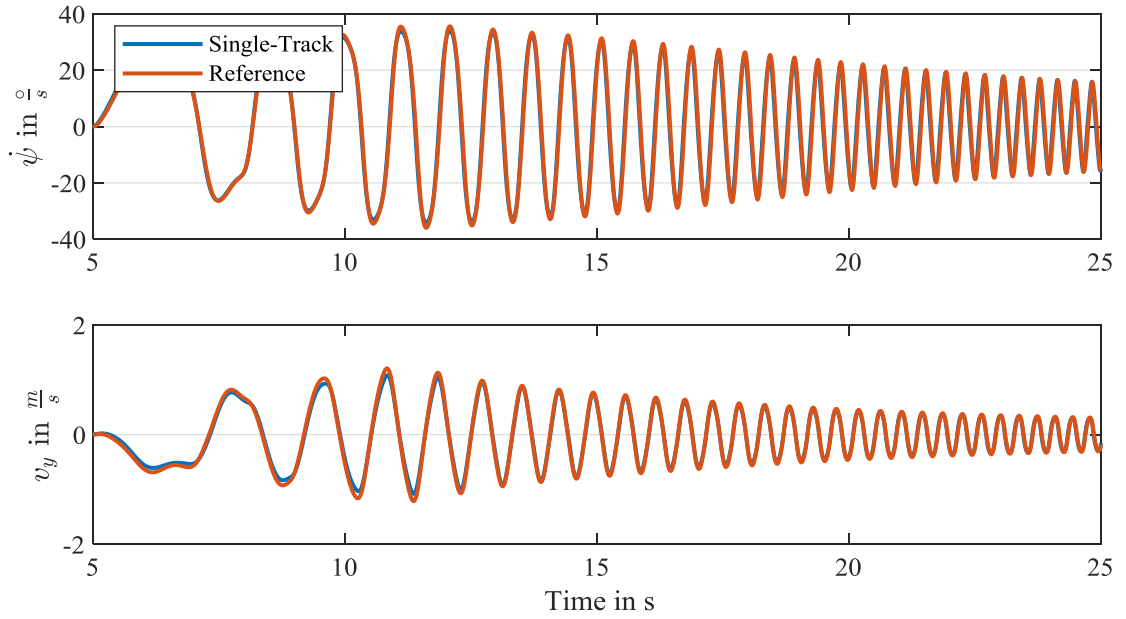


Figure 29: Results of identification for sine chirp maneuver on $\mu = 1$

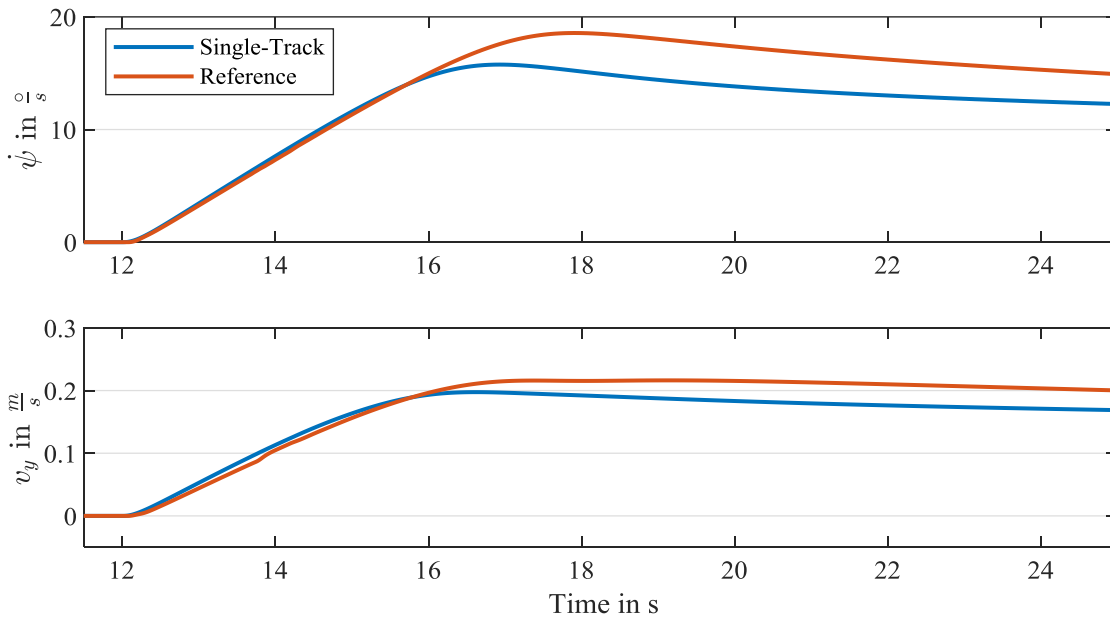


Figure 30: Results of identification for Semi-Steady-State circle on $\mu = 0.4$

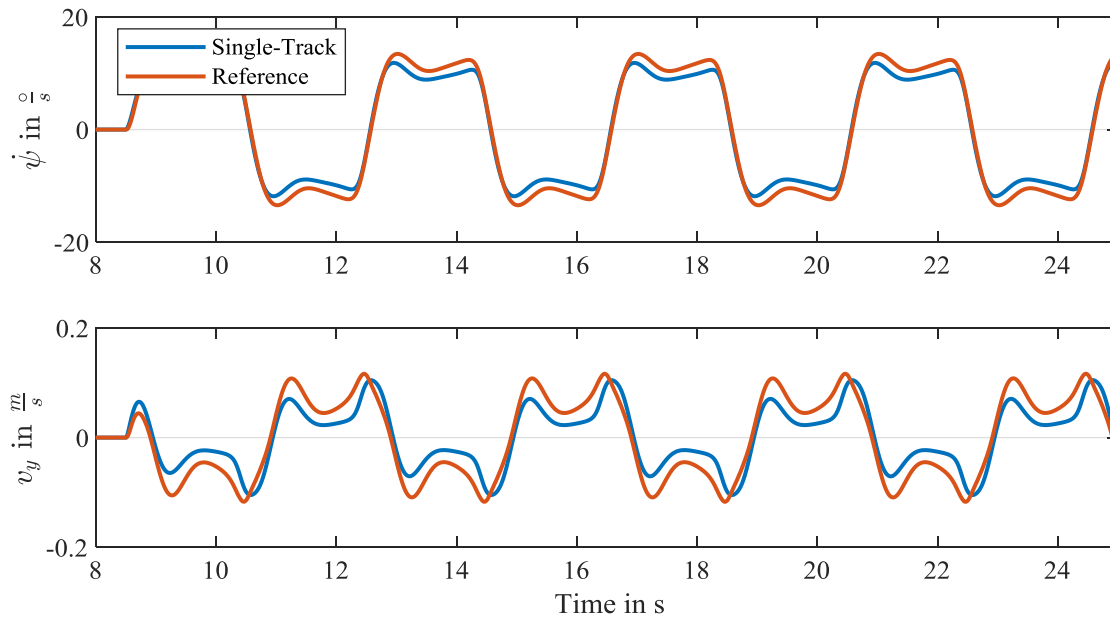


Figure 31: Results of identification for constant sine wave maneuver on $\mu = 0.4$

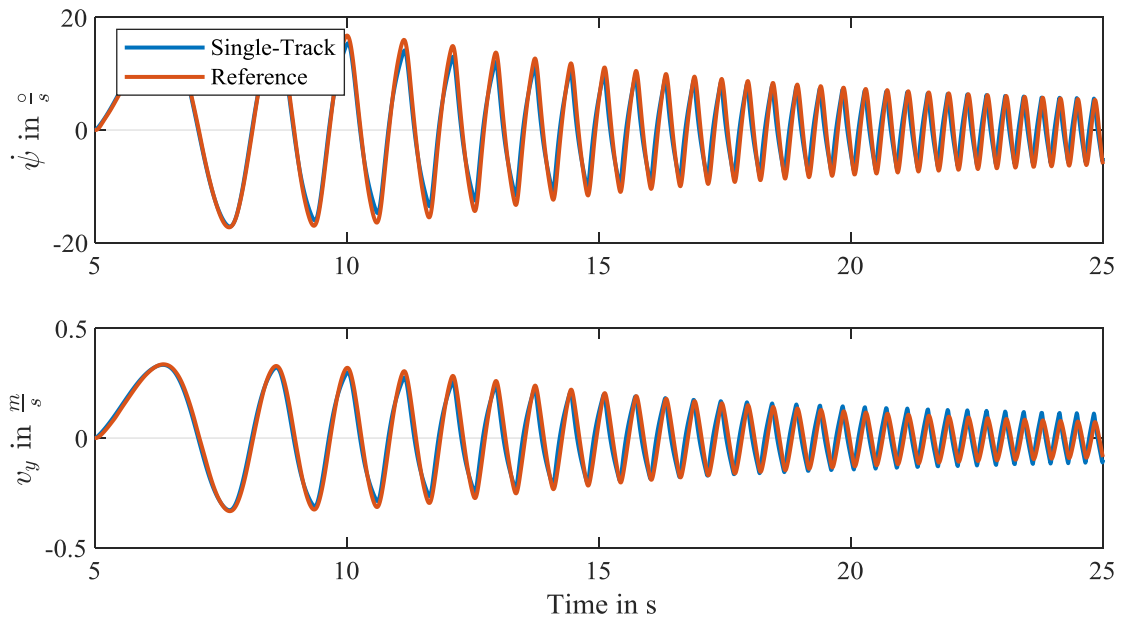


Figure 32: Results of identification for sine chirp maneuver on $\mu = 0.4$

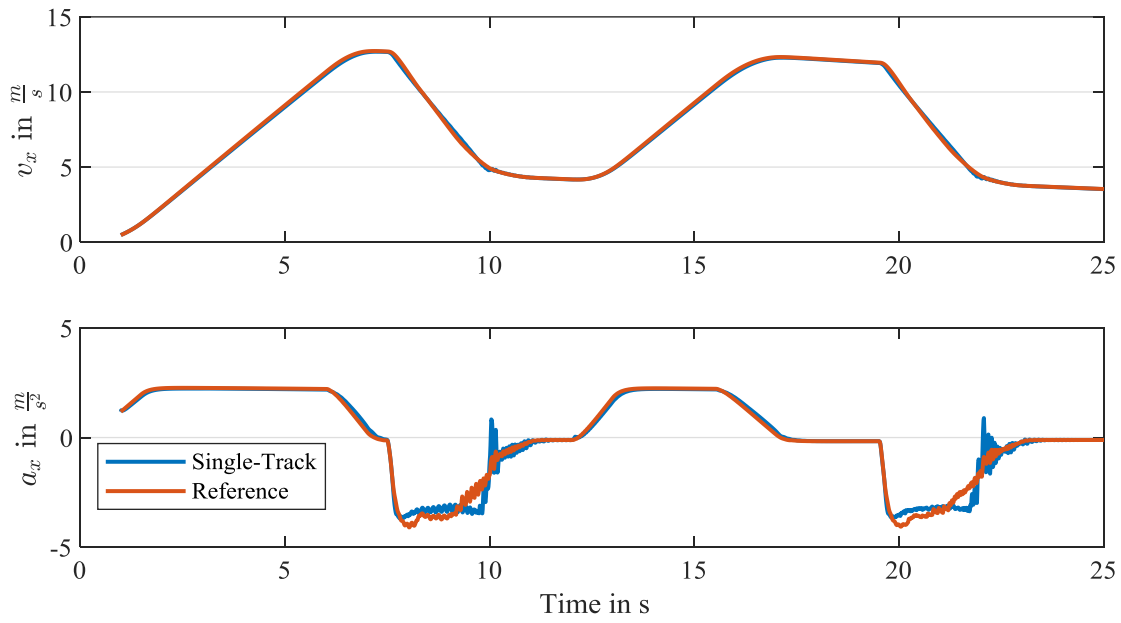


Figure 33: Results of identification for emergency braking maneuver on $\mu = 0.4$

A.2 All Results EKF Identification

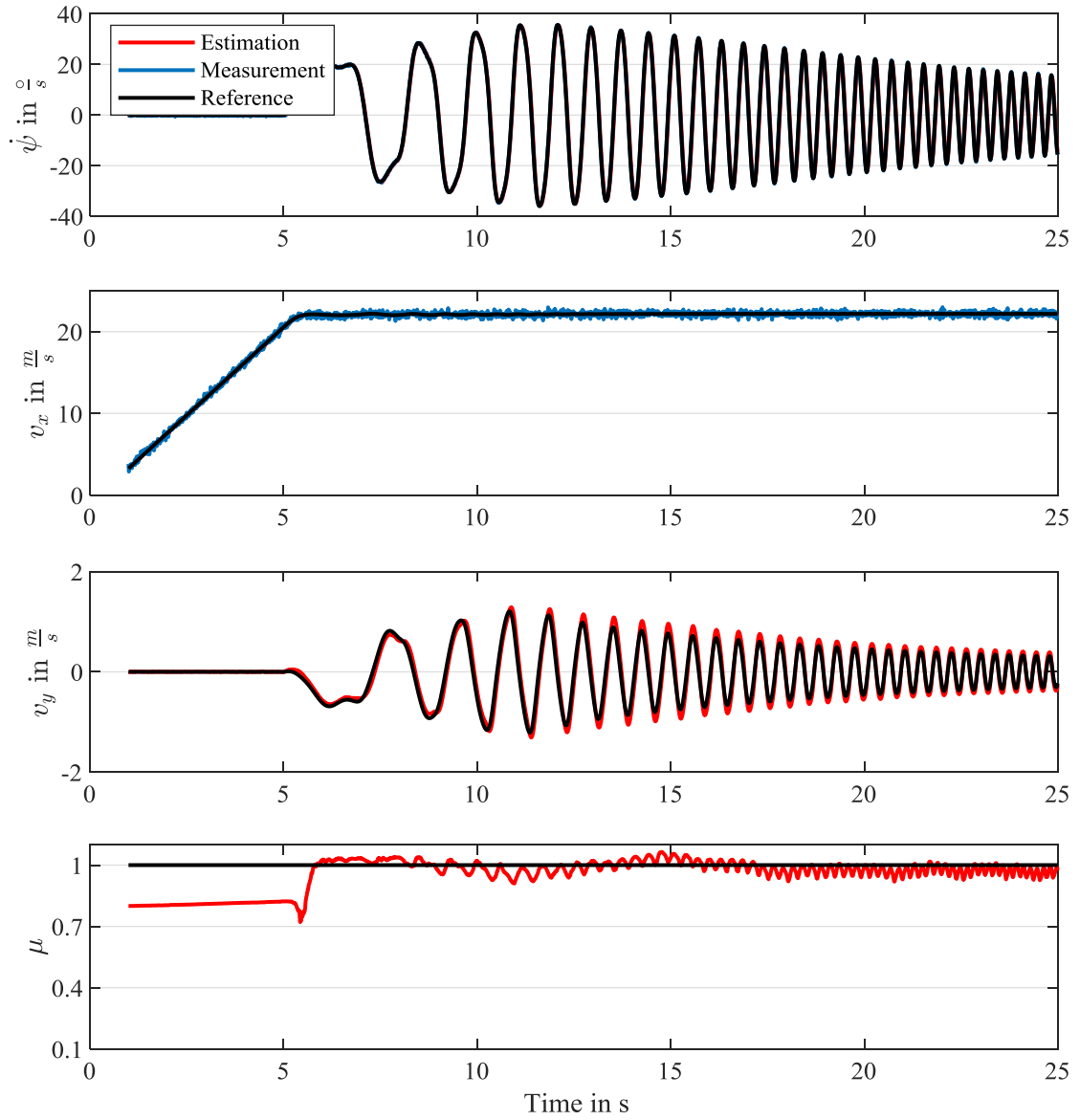


Figure 34: Results of μ estimation for sine chirp maneuver on $\mu = 1$

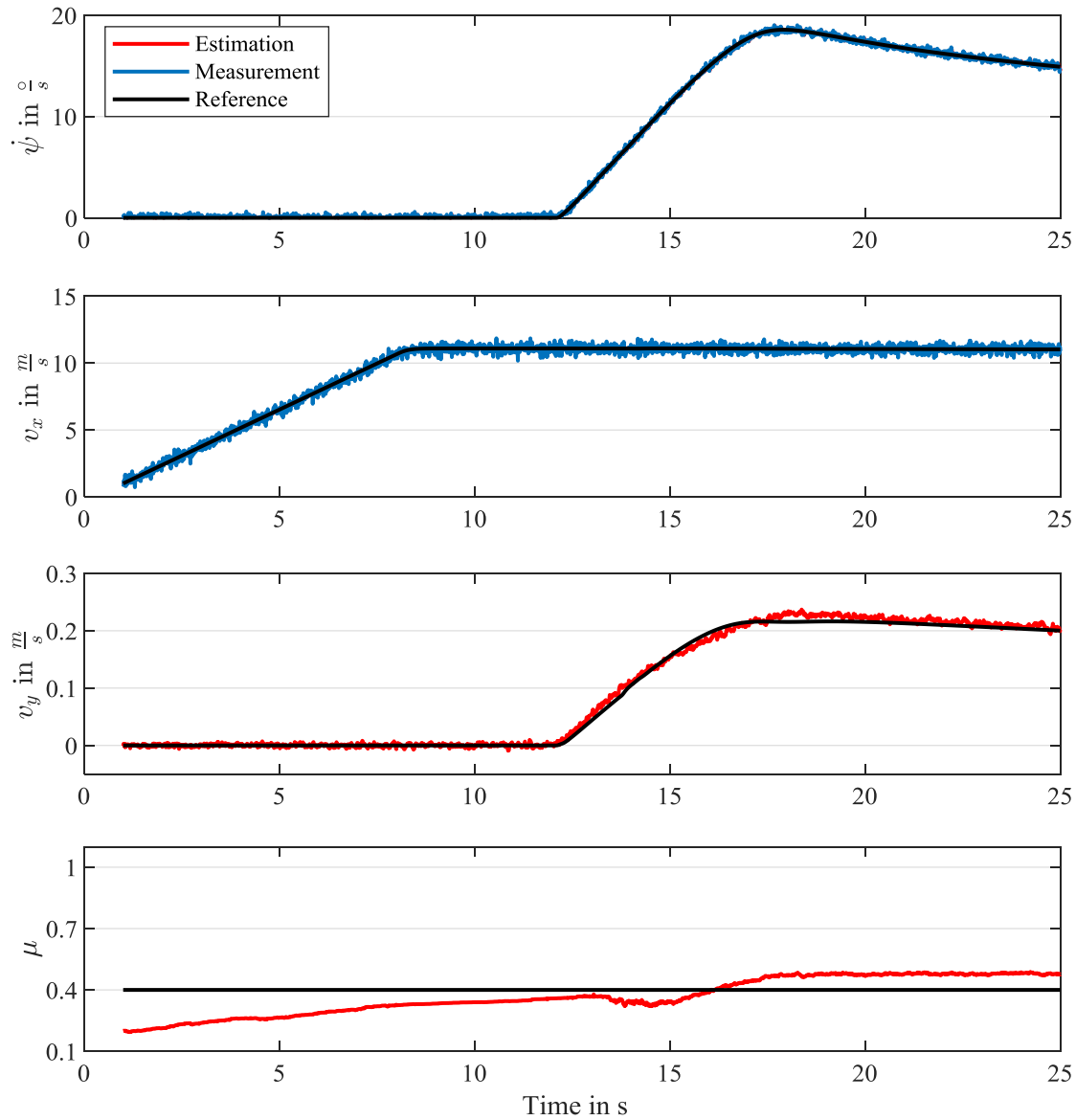


Figure 35: Results of μ estimation for semi-steady-state circle maneuver on $\mu = 0.4$

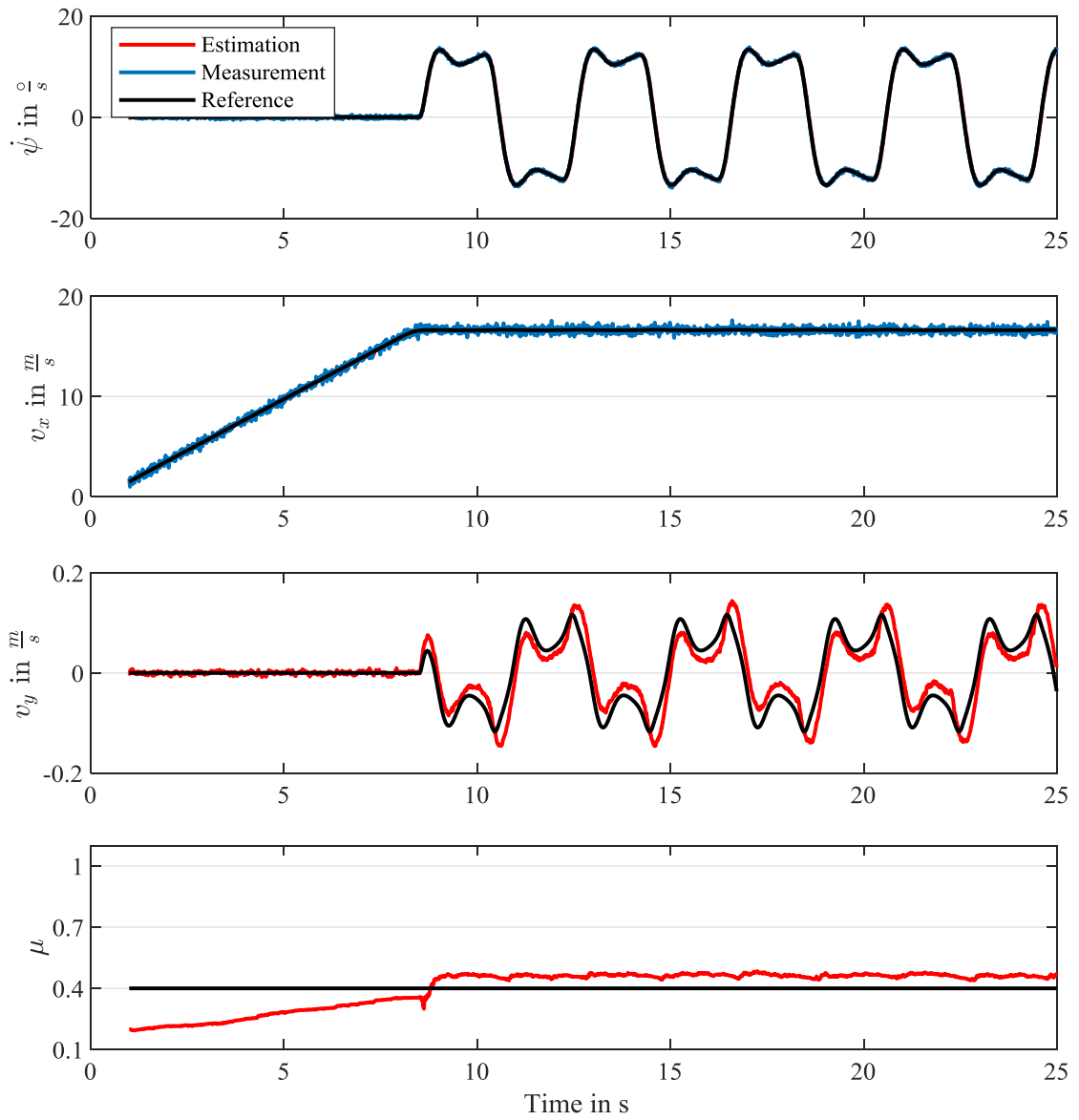


Figure 36: Results of μ estimation for constant sine wave maneuver on $\mu = 0.4$

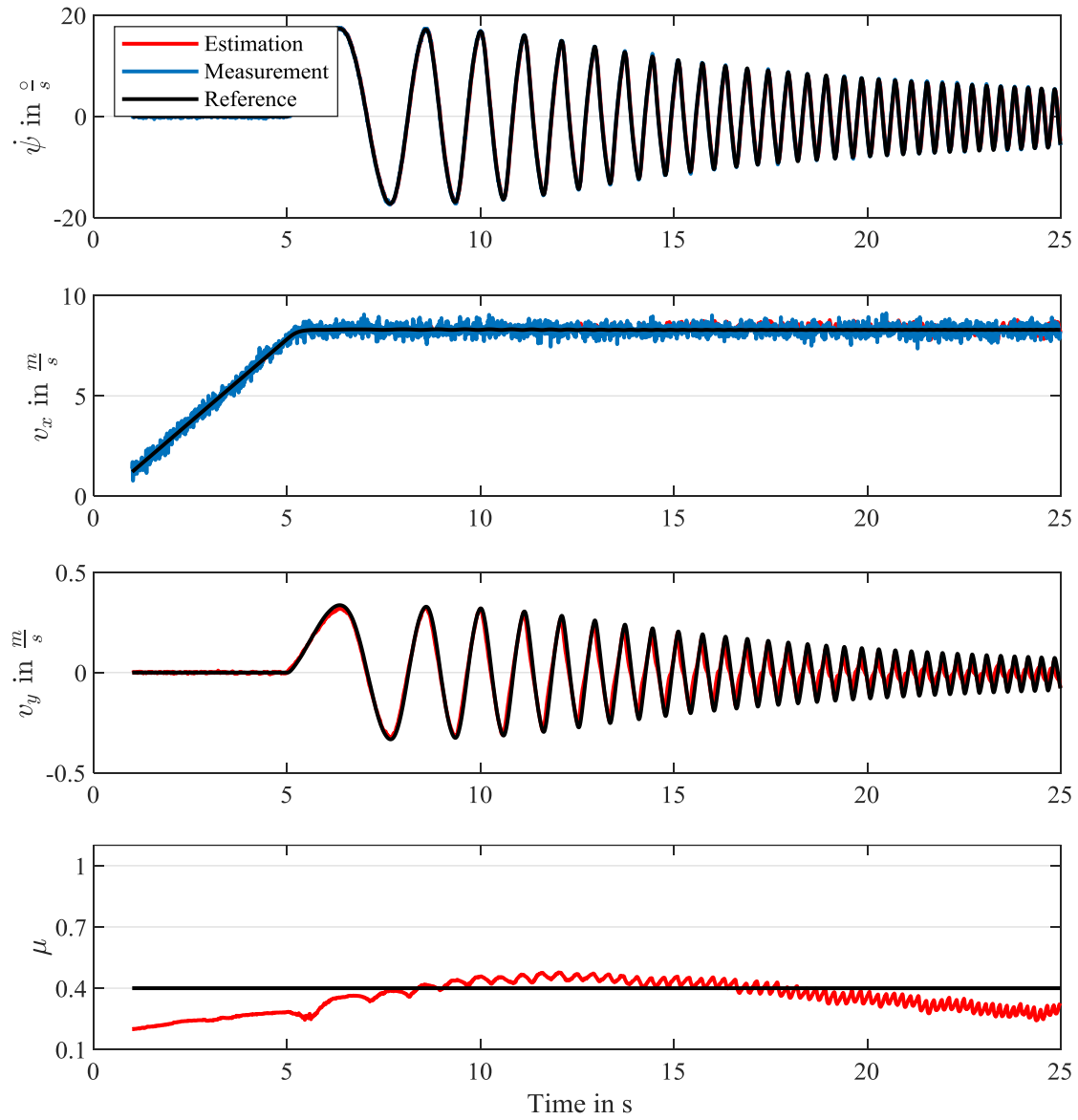


Figure 37: Results of μ estimation for sine chirp maneuver on $\mu = 0.4$

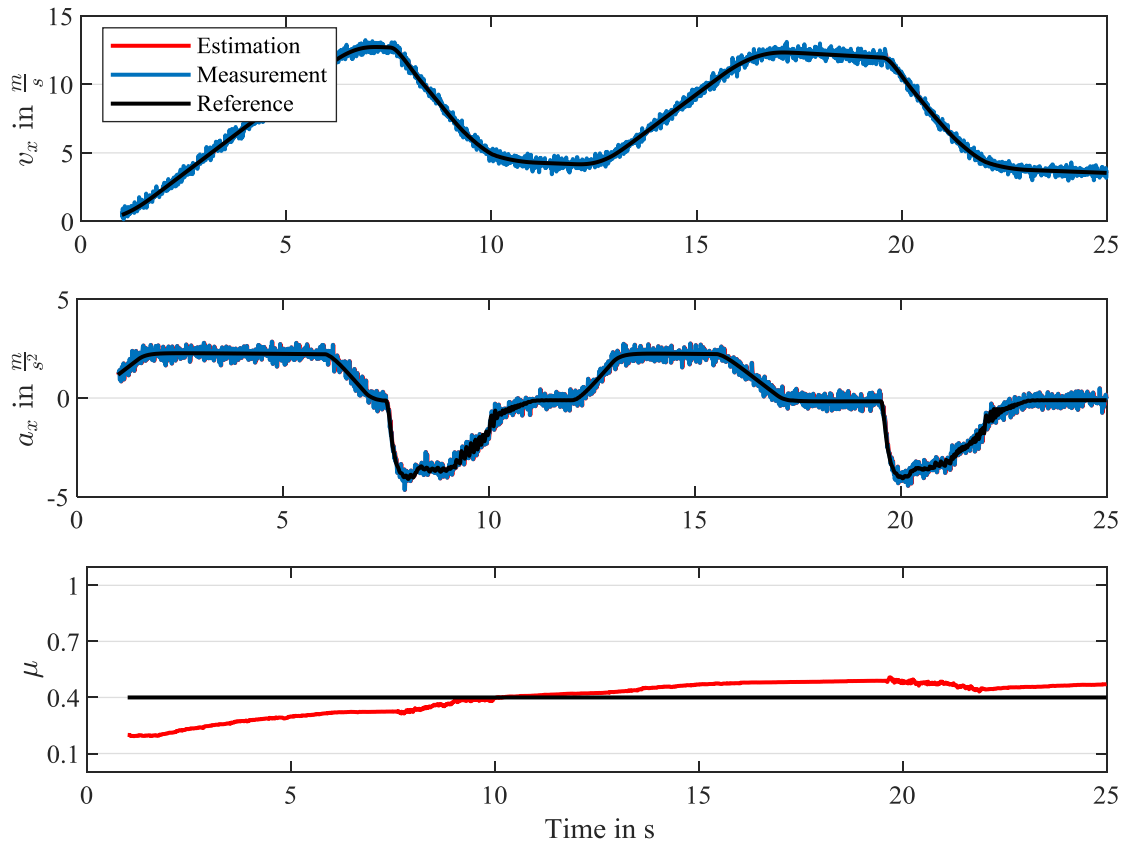


Figure 38: Results of μ estimation for emergency braking maneuver $\mu = 0.4$

REFERENCES

- [1] S. Khaleghian, A. Emami und S. Taheri, „A technical survey on tire-road friction estimation,“ Springer, Wiesbaden, Germany, 2017.
- [2] C. You and P. Tsiotras, "Vehicle Modeling and Parameter Estimation Using Adaptive Limited Memory Joint-State UKF," in *2017 American Control Conference*, Seattle, USA, 2017.
- [3] M. Gerard, „Tire-Road Friction Estimation Using Slip-based Observers,“ Lund University, Lund, Sweden, 2006.
- [4] K.-U. Henning, *Integrierte Querdynamikregelung eines überaktuierten Kraftfahrzeugs*, Aachen, Germany: Shaker Verlag, 2018.
- [5] M. C. Best, „Identifying Tyre Models Directly from Vehicle Test Data using an Extended Kalman Filter,“ Taylor and Francis, Loughborough, United Kingdom, 2010.
- [6] S. Garatti und S. Bittanti, „Parameter estimatin in the Pacejka's tyre model through the TS mehod,“ Politecnico di Milano, Milano,Italy, 2009.
- [7] E. Narby, „Modeling and Estimation of Dynamic Tire Properties,“ Linköping University, Linköping, Sweden, 2006.
- [8] The MathWorks, Inc., „Vehicle Dynamics Blockset,“ [Online]. Available: <https://de.mathworks.com/help/vdynblks/index.html>. [Accessed on July 7 2019].
- [9] H. Hamann, J. K. Hedrick, S. Rhode und F. Gauterin, „Tire force estimation for a passenger vehicle with the Unscented Kalman Filter,“ in *2014 IEEE Intelligent Vehicles Symposium Proceedings*, Dearborn, USA, 2014.
- [10] D. Schramm und R. Bardini, *Vehicle Dynamics*, Heidelberg, Germany: Springer, 2018.
- [11] S. Haykin, *Kalman Filtering & Neural Networks*, Hamilton, UK: John Wiley & Sons, Inc., 2001.
- [12] R. Marchthaler und S. Dingler, *Kalman-Filter*, Wiesbaden,Germany: Springer Vieweg, 2017.

- [13] A. Iggidr, „Controllability, Observability and Stability of Mathematical Models,“ Eolss Publishers, Metz, France, 2013.
- [14] The MathWorks, Inc., „fmincon,“ [Online]. Available: <https://de.mathworks.com/help/optim/ug/fmincon.html>. [Accessed on June 28 2019].
- [15] The MathWorks, Inc., „Constrained Nonlinear Optimization Algorithms,“ [Online]. Available: <https://de.mathworks.com/help/optim/ug/constrained-nonlinear-optimization-algorithms.html>. [Accessed on June 28 2019].
- [16] M. Decker, Zur Beurteilung der Querdynamik von Personenkraftwagen, München, Germany: Technische Universität München, 2009.
- [17] M. Unterreiner, Modellbildung und Simulation von Fahrzeugmodellen unterschiedlicher Komplexität, Duisburg, Germany: Universitätsbibliothek Duisburg-Essen, 2014.
- [18] D. Kollreider, Identifikation der Reifeneigenschaften als Grundlagen zur Fahrdynamikbewertung, Graz, Austria: TU Graz, 2009.

